This is the peer-reviewed, final accepted version for American Mineralogist, published by the Mineralogical Society of America.
The published version is subject to change. Cite as Authors (Year) Title. American Mineralogist, in press.
DOI: https://doi.org/10.2138/am-2021-7656. http://www.minsocam.org/

# Revision 1

# Early Archean alteration minerals in mafic-ultramafic rocks of the Barberton greenstone belt as petrological analogues for clay mineralogy on Mars

Eugene G. Grosch[1], Janice L. Bishop[2], Christian Mielke[3], Alessandro Maturilli[4], Joern Helbert[4]

[1]Rhodes University, Geology Department, Grahamstown, South Africa

[2]Carl Sagan Center, SETI Institute and NASA-Ames Research Center, Mountain View, CA

[3]GFZ German Research Centre for Geosciences, Telegrafenberg, 14473 Potsdam

[4]Institute for Planetary Research, DLR (Rutherfordstrasse 2, 12489, Berlin-Adlershof, Germany, alessandro.maturilli@dlr.de), Potsdam.

Submitted to: *American Mineralogist* Special Issue on: EARTH ANALOGUES FOR MARTIAN GEOLOGICAL MATERIALS

## Abstract

Characterization of terrestrial analogue sites is critical for detection and determination of clay mineralogy in remote sensing studies of Mars aimed at geological, hydrological and potentially biological investigations. In this study, we investigate a suite of hydrothermally altered early Archean rocks from the Barberton greenstone belt (BGB) of South Africa as potential petrological, mineralogical and spectral analogues to hydrothermally altered metabasalts and mafic-ultramafic intrusions in the martian subsurface and impact craters. We present the first spectral imaging measurements on exceptionally well-preserved early Archean mafic-ultramafic rocks from the BGB, with the aim of studying their clay mineralogy and spectral signatures. Multiple spectral analyses were conducted on different sample textures (rock powders, crushed rocks, and rock slabs) appropriate for Mars rover and remote sensing exploration. Visible/near-infrared (VNIR) and mid-IR reflectance spectra were acquired on particulate samples, while VNIR spectral imaging data were collected on rock slabs. Mid-IR emission spectra were measured for the rock slabs and grains. Spectral features are compared from these different

spectral techniques in order to identify the minerals present in the samples and compare macroscale versus microscale detections. The measured spectra reveal absorption bands that correspond to clay mineralogy of the serpentine and chlorite mineral groups, consistent with petrographic observations, as well as magnetite, olivine, quartz, feldspar and Al-phyllosilicate. The spectral data acquired in this study expand the reference spectra dataset for remote sensing studies. The implications of this study are that rocks from early Archean greenstone belts, such as those of the BGB, serve as potential clay-bearing petrological analogues for hydrothermal environments on Mars.

**Keywords:** Barberton greenstone belt, early Earth, Archean metabasalts, Mars petrological analogues

## 1. Introduction

In the search for life on Mars, "follow the water" has been a validated and useful approach. The main indicator of surface and subsurface groundwater on Mars is the presence of low-temperature alteration minerals such as phyllosilicates, opal, zeolite and sulfate (e.g., Murchie et al., 2009; Carter et al., 2013; Ehlmann and Edwards, 2014). Orbital remote sensing missions and Mars rover observations have found evidence for alteration and clay formation in multiple surface and subsurface environments including a variety of hydrothermal conditions (e.g., Ehlmann et al., 2009, 2010, 2011a, 2013; Marzo et al., 2010; Squyres et al., 2012; Bishop et al., 2013a; Michalski et al., 2013, 2017; Bridges et al., 2015; Bristow et al., 2015). These studies report *in situ* and hyperspectral data in support of the relatively common occurrence of (Fe, Mg)-rich phyllosilicates (e.g., smectite, chlorite, and serpentine) and Al-rich phyllosilicates (kaolinite, montmorillonite) on the exposed surface of Mars. Lab spectra of clay–bearing rocks from various hydrothermal settings on Earth (e.g., Bishop et al., 2002, 2005, 2007; Michalski et al., 2006; Schiffman et al., 2006; Hamilton et al., 2008; Ehlmann et al., 2011b, 2012; Cuadros et al., 2013; Yant et al., 2018) provide important constraints on geochemical conditions, temperature, type of salts and nature of water activity on Mars. Furthermore, sub-surface mafic-ultramafic hydrothermal environments on early Earth and Mars may have been very similar (e.g. Cockell et al., 2006; Izawa et al., 2019; Grosch and Hazen, 2015). Investigation of Fe/Mg-rich clays from

seafloor sites (Cuadros et al., 2013) has led to characterization of distinct types of clays on Mars (Michalski et al., 2015; Bishop et al., 2018). Consequently, clay-bearing early Archean terrestrial rocks may be useful as analogue materials to extend the visible/near-infrared (VNIR) and mid-infrared (mid-IR) spectral databases for remote sensing studies on orbital and rover missions at Mars. It is important to point out that clay mineral formation processes on early Earth and Mars may not necessarily have been the same in all geological environments, and we propose that the Barberton rocks are possible petrological analogues, not necessarily direct alteration process analogues. However, the early sub-surface hydrothermal environments may have been similar in some parts on early Earth and Mars.

Bioalteration of basaltic volcanic glass is a model that has been invoked to explain the occurrence of granular and tubular microstructures in modern and ancient volcanic glass (Thorseth et al. 1995, Fisk et al. 1998, Furnes et al. 2001). In this model, chemolithoautotrophic micro-organisms are believed to be involved in accelerating glass dissolution for nutrients and energy producing microborings (e.g. Thorseth et al., 1995). In the modern oceanic crust, the existence of a subseafloor biosphere is supported by a range of evidence that includes microbiological data, sulphur and carbon isotopes, and detailed reviews of this body of evidence can be found in Orcutt et al. (2011), Edwards et al. (2011), and Thorseth (2011). Titanite microstructures in ophiolite and Archean pillow lavas have also been argued to represent early microborings by mico-organisms thriving in the Archean subseafloor environment (Furnes et al. 2004, Banerjee et al. 2007, Staudigel et al. 2008), although the biogenicity and syngenicity of these structures have been brought into question by Grosch and McLoughlin (2014). However, it is not impossible, that the oceanic hydrothermal subsurface was a habitat for the earliest microbial life protected from harsh UV rays on early Earth. This has important astrobiological implications as it would suggest that early mafic-ultramafic hydrothermal subsurface environments beneath martian impact craters may have been favorable sites for microbial life to thrive (e.g. Cockell et al., 2006). As a hypothesis, the hydrothermal mafic-ultramafic subsurface environments on early Earth and early Mars may both have been potentially habitable sites, particularly given the evidence for water on early Mars (e.g., Craddock and Howard, 2002; Cockell et al., 2006, Grosch and Hazen, 2015, Izawa et al., 2019).

The 3.55 to 3.10 billion-year-old rocks of the early Archean Barberton greenstone belt (BGB) volcano-sedimentary succession represent an exceptionally well preserved rock archive of early Earth processes. In this study, we make the case that altered, silicified, serpentinized and clay-bearing mafic-ultramafic rock samples from the early Archean BGB, may prove to be useful petrological analogues for low-temperature martian environments. Hydrogen production from low-temperature alteration of ultramafic and basaltic rocks has been proposed to support early microbial life in Earth's earliest subsurface environments, which may have been the case for early Mars (Oze and Sharma, 2005; Grosch and Hazen, 2015). Investigation of serpentines on Mars has also received attention as a potential source of $H_2$ and methane that could have supported microbial life (Ehlmann et al., 2010; Mustard and Tarnas, 2017). Archean terrestrial rock environments preserved in greenstone belts may play an important role in understanding early martian subsurface environments relevant to the search for extra-terrestrial life and water. Previous studies have successfully provided hyperspectral maps of altered, clay-bearing outcrops in the early Archean North Pole Dome of the Pilbara Craton (Brown et al., 2004; 2007). In this context, the rock sequences of the Paleoarchean BGB of South Africa provide unique martian analogues as these rocks are exceptionally well preserved and record early Earth surface and subsurface processes that could be related to processes on early Mars as well. Geological evidence for early Archean sedimentary delta fan deposits (Drabon et al., 2019), storm-reworked volcanic deposits (Trowera and Lowe, 2016) and spherule beds marking violent meteorite impacts (Lowe et al., 2003; 2014) have all been reported from the Barberton greenstone belt. *In situ* exploration by rovers, remote sensing studies, and meteorite evidence has indicated the presence of metabasalts, altered gabbros, olivine-/pyroxene-bearing basalts, serpentinized picritic basalts or peridotites on Mars.

In this study we present spectra of several 3.4 to 3.5 billion-year-old Archean mafic-ultramafic greenstone belt rock samples as analogue materials that include chloritized and silicified tholeiitic basalts, basaltic komatiites, serpentinized ultramafic komatiites and a felsic tonalite (see Table 3). These Archean BGB samples were characterized petrologically in previous studies (e.g. Grosch et al. 2012; Bost et al., 2013). The field setting on an outcrop scale, petrography and mineralogy of the Archean BGB samples are presented here. Mineral composition data on relic igneous and clay mineral phases are discussed in context with the spectroscopy results. We have analyzed VNIR and mid-IR reflectance spectra and mid-IR

118 emission spectra on these early Archean samples with the aim of using these spectra for ground
119 truthing remote sensing data and performing mineral identification and characterization of
120 alteration environments on Mars. Specifically, the VNIR spectra cover the spectral range
121 collected by CRISM (Compact Reconnaissance Imaging Spectrometer for Mars, Murchie et al.,
122 2009) on the Mars Reconnaissance Orbiter (MRO) and the MicrOmega instrument (Bibring et
123 al., 2017) planned for ESA's ExoMars rover. The mid-IR spectra cover the spectral range
124 measured by TES (Thermal Emission Spectrometer, Christensen et al., 2001) on the Mars Global
125 Surveyor orbiter as well as the Mini-TES spectrometer on board the Mars Exploration (MER)
126 rovers (e.g.,Christensen et al., 2003; Ruff et al., 2019). VNIR reflectance spectra acquired of
127 individual rock surfaces and size fractions are compared to VNIR reflectance imaging of rock
128 surfaces. This study provides an opportunity to evaluate alteration on ancient Earth rocks and
129 provides spectral data sets to search for related phyllosilicates and hydrous minerals on Mars.

130

131 **2. Barberton early Earth analogue sites for Mars**

132 The Paleoarchean BGB hosts some of the world's best preserved rocks of the early Archean eon
133 and some of the earliest traces of microbial life preserved in shallow silicified seafloor
134 sediments, known as cherts (Walsh, 1992;) and potentially in volcanic subseafloor environments
135 (Mcloughlin et al., 2012 and references therein). Exceptionally well preserved tectonic slivers of
136 altered Mesoarchean oceanic crust and associated sediments have been identified, providing a
137 unique mineralogical and petrological archive of information related to the evolution of early
138 Earth (Grosch et al., 2012). For these reasons the early Archean BGB rocks have been at the
139 center of a number of international scientific drilling projects (e.g., Grosch et al., 2009, Philipott
140 et al., 2009).

141 This study focuses on rocks from the 3.55 to 3.33 Ga Onverwacht Group of the BGB (see
142 simplified geological map in Figure 1 a-c with U-Pb zircon constraints). A number of early
143 Archean mafic-ultramafic hydrothermal environments have been identified, particularly in the
144 oldest part of the BGB stratigraphy related to shallow subsurface hydrothermal activity (e.g.,
145 Hanor and Ducaq, 1990; Hofmann and Harris, 2008). Retrograde alteration and sheet silicate
146 formation has also been recorded in mafic-ultramafic tectonite zones (Grosch et al., 2009; 2012).

Various metabasaltic and serpentinized ultramafic field outcrops of the Onverwacht Group are shown in Figure 1 (d–h) representing examples of a wide range of early Archean low-temperature hydrothermal settings on early Earth potentially useful as analogue sites to martian environments.

Coarse-grained cumulate metaperidotites are commonly found in the BGB. These include ultramafic intrusions and mantle-derived rocks (Furnes et al., 2011, Grosch et al., 2012). An example of such rock types is the layered serpentinized, olivine-rich meta-dunite of the 3.3 Ga Kromberg Formation of the mid-Onverwacht Group (see Figure 1d). Other examples of serpentinized peridotitic mantle rocks include the ultramafic meta-dunite complex of the 3.47 Ga upper Komati Formation (Dann, 2000). Metadunites and metaperidotites are considered in this study as analogues for coarse-grained ultramafic cumulate rocks or mantle-derived rocks on Mars. The Onverwacht Group largely consists of tholeiitic metabasalt flows and pillow lavas. Pillow lava metabasalts of the 3.53 billion-year-old Theespruit Formation have been metamorphosed to upper greenschist/amphibolite facies conditions and are moderately deformed (Figure 1f). These pillow metabasalts also have mica and amphibole as part of their metamorphic assemblage. Other oceanic pillow lava flows in the structurally overlying 3.47 Ga Hooggoenoeg Formation and 3.3 Ga Kromberg Formation are exceptionally well-preserved, recording early subseafloor magmatic and hydrothermal conditions (Figure 1e). Metamorphic alteration temperature conditions in these rocks could be as low as ca. T = 140 $^{o}$C (Grosch et al. 2012). Metabasaltic flows in the Hooggenoeg, Kromberg and Mendon Formations also record evidence for low-temperature ca. 80 – 150 $^{o}$C subseafloor silicification beneath overlying oceanic sediments (Hanor and Ducaq, 1990; Hofmann and Harris, 2008). Metabasaltic alteration environments on Mars similar to these silicified basalts would be acid-sulphate leaching by sulphate-rich groundwater brines at low-temperature conditions. Most of the metabasaltic flows in the BGB consist of chloritized basalts (Figure 1e) and altered basaltic komatiites, possibly similar to hydrothermally produced crustal chlorite in the subsurface of Mars (see Ehlmann et al., 2011a,). The typical major element bulk rock composition of a metabasalt from the BGB is provided in **Table 1**. This composition is compared to those of the martian metabasalts Chesterlake and Deadwood measured by the Mars Exploration Rover (MER) Opportunity at Endeavour Crater (Squyres et al., 2012, **cf. Table 1**). A strong similarity in whole-rock metabasalt composition is observed between these rocks. For this reason, further investigation of

the metabasalts and serpentinites from the BGB were undertaken with the goal of providing geochemical constraints on the formation environments for related metabasalts on Mars.

The BGB is also the site of ultramafic volcanic rocks known as komatiites (Viljoen and Viljoen, 1969b), which are generally considered to represent hotter mantle conditions on the early Earth. These rocks can be spinifex-textured due to the presence of elongated olivine or pyroxene hopper crystals. Ultramafic komatiites can be olivine- or pyroxene-rich. An olivine-spinifex komatiite from the 3.48 Ga Komati Formation of the BGB is shown in Figure 1g. Komatiites are typically altered by silicification or serpentinization. Serpentinized komatiites and komatiitic basalts typically contain the alteration assemblage chlorite + antigorite + brucite. Other serpentine minerals can also be present such as chrysotile. We propose that serpentinized komatiites from the BGB region may help understand serpentinized ultramafic rocks exposed on Mars. Serpentine has been observed in mélange terrains with olivine and other phyllosilicates at Claritas Rise and Nili Fossae, in small outcrops of the central peaks, walls or ejecta of a few impact craters, and associated with olivine and Mg-carbonate in Noachian rocks underneath a Hesperian flow in northern Syrtis Major west of the Isidis impact basin (Ehlmann et al., 2010). Carbonate + quartz + fuchsite (Cr-rich mica) + chlorite alteration horizons (Figure 1h) have also been identified in komatiites, basaltic komatiites, metagabbros and metaperidotites (e.g,, Hanor and Ducaq, 1990; Hofmann and Harris, 2008, Grosch et al., 2012). These typically occur in retrograde tectonic shear zones (Grosch et al., 2012). Given the high $CO_2$ activity in martian groundwater brines (Michalski et al., 2013), these carbonate and sheet silicate BGB hydrothermal alteration sites may also prove to be useful analogues for altered olivine-bearing rocks on Mars such as those across the Nili Fossae region, in the flows of Syrtis Major, surrounding the Isidis impact basin, and associated with smaller craters (e.g., Hamilton and Christensen, 2005; Mustard et al., 2005, 2009; Bishop et al., 2013; Michalski et al., 2019).

## 3. Methods

### 3.1 Sample Preparation

A list of the 11 rock samples analyzed in this study is provided in **Table 2**. This includes the BGB rock formation where the sample was collected (see Map in Figure 1) and the

corresponding GPS co-ordinates. Multiple samples were prepared for each rock of interest in the rock preparation lab at the University of Bergen, Norway. For each hand specimen sample, a thin section (24 mm wide by 48 mm long and ca. 38 micron thick) was prepared for petrographic analysis and mineral identification (Grosch et al., 2012). Portions of each sample were crushed to prepare coarse-grained samples by using a jaw crusher, which produced rock chips approximately 0.3 - 0.8 mm in diameter. Additional samples were further pulverized into rock powers using a clean agate mill. Using a rock saw, rock slabs were cut for selected samples with dimensions of ca. 25 by 50 mm for the HySpex VNIR spectral scanning.

### 3.2 Sample Petrography

Photomicrographs of representative samples and associated alteration assemblages are shown in Figure 2. The metadunite sample (KM-dun) from the ca. 3.49 Ga upper Komati Formation displays a coarse-grained texture consisting mainly of subhedral olivine grains replaced by low-temperature serpentine alteration minerals (Figure 2a). A two-stage alteration pattern is present with the cores of former olivine grains altered to fine-grained serpentine and magnetite that is, in turn, surrounded by outer rims of chlorite (clinochlore). Relic igneous phases could not be identified and the sample displays a high degree of chloritization. The serpentinized spinifex komatiite sample (KM-spin18) consists of elongated, olivine hopper crystals as well as dendritic and plumose olivine crystal aggregates in the matrix between elongated spinifex blades (Figure 2b). The olivine hopper crystals are extensively altered mainly to chlorite and magnetite with minor serpentine, whereas the finer-grained crystals in the matrix are largely replaced by serpentine. The altered komatiite sample (KM-2c) consists mainly of olivine replaced by brucite and antigorite (high temperature serpentine), with a rim of carbonate (dolomite) and quartz (Figure 2c). Antigorite veins in this sample display extensional cross-fibers (Figure 2c).

The serpentinized ultramafic komatiite sample (KM-K6) contains olivine replaced by fine-grained antigorite and minor lizardite (low temperature serpentine), cross-cut by chlorite and lizardite veins (Figure 2d). Magnetite, carbonate (dolomite) and quartz are present with chlorite in the altered interstitial groundmass. The metabasaltic sample from the ca. 3.47 Ga Hooggenoeg Formation (HC3) features chloritized volcanic glass from a chilled pillow lava rim. The low-

temperature alteration assemblage in this sample consists of green chlorite plus epidote, with accessory titanite and quartz (Figure 2e). Sample HC3 contains the typical subgreenschist facies assemblage found in metabasalts from the BGB, although actinolitic amphibole is also frequently present in pillow lava metabasalts that have experienced greenschist facies conditions (Grosch et al., 2012). An extensively altered metabasalt from the ca. 3.55 Ga Theespruit Formation in the oldest part of the BGB (THS-4) consists mainly of coarse tabular grains of Cr-rich chlorite, magnetite and sulphides (Figure 2f). An altered felsic rock from the Kaap Valley Tonalite intrusion (KV1) is included as a control sample for comparison with the mafic-ultramafic rock types and enables the study of sericitized plagioclase and chloritized amphibole.

### 3.3. *Reflectance spectra of BGB samples*

Reflectance spectra were acquired using two systems. VNIR spectra were measured from 0.35-2.5 μm under ambient conditions on rock surfaces, coarse-grained rock fragments, and rock powders (ground with a ball mill system to ~<125 μm) using an ASD FieldSpecPro spectrometer at the SETI Institute. Reflectance spectra were also measured on the particulate samples at RELAB at Brown University from 0.3 to 50 μm as in past studies (e.g. Bishop et al., 2008). The spectra are a composite of bidirectional spectra collected under ambient conditions at 5 nm spectral resolution from 0.3-1.3 μm relative to Halon and biconical FTIR spectra collected using a Nicolet spectrometer under a dehydrated environment (purged of $H_2O$ overnight) at 4 $cm^{-1}$ spectral resolution from 1-50 μm relative to a rough gold surface.

### *3.4. Mid-IR emission spectra of BGB samples*

Emissivity measurements were conducted in the Planetary Emissivity Laboratory (PEL) at the German Aerospace Center (DLR) in Berlin, Germany. Details on the laboratory set-up, equipment, measurements methods and calibration procedures can be found in Maturilli et al. (2019). To measure emissivity, samples were heated in two custom-designed external emissivity chambers, each of them attached to a Bruker Vertex80V FTIR spectrometer and spectra were collected from ~630-4000 $cm^{-1}$ (or 2.5 to 16 μm) for these experiments. The samples were

heated under purged air in an emissivity chamber attached to one of the FTIR spectrometers at PEL. Each sample was positioned in an aluminum cup and heated for one hour to reach the temperatures steps of 20 °C, 50 °C, and 100 °C. The emissivity chamber walls were water-cooled to 5 °C during the sample measurements to minimize the spectral signature of the chamber measured at the detector. Successively, the same samples have been heated under vacuum in a second emissivity chamber, attached to another FTIR spectrometer. The whole optical path between the sample and the detector was under vacuum (0.7 mbar). A thermocouple was in contact with the sample surface to allow heating of the samples at the desired temperatures of 50 and 100 °C. All the samples measured in emissivity have been calibrated against an Acktar Fractal Black™ blackbody, measured under exactly the same conditions as the samples.

### *3.5. Spectral imaging of rock slabs using HySpex*

The rock slabs were scanned using the hyperspectral imaging spectrometer system (HySpex) at the GFZ Potsdam (Baarstad et al., 2005). The HySpex system uses two cameras: the VNIR 1600 covers the range 400 - 1000 nm and the 320m-e covers the range1000 nm – 2500 nm. The samples are moved through the field of view of both cameras via a precision translation stage. This allows recording an image scene over the range 400-2500 nm. Both line scan cameras, the translation stage, and the light source (Hedler studio light with 1600 W) are mounted in a laboratory rack that allows the use of different foreoptics and measurement distances for the HySpex cameras. For this study we selected lenses optimized for a distance of 30 cm above the sample. The geometric correction and reflectance retrieval is carried out with an in-house preprocessing chain that combines fast Fourier transform techniques (Xie et al., 2003) with scale invariant feature transformation (SIFT) techniques (Vedaldi et al., 2008) for image registration and a manual delineation of the reflectance panel for irradiance normalization and reflectance retrieval.

Automated mineral mapping from large imaging spectroscopy datasets was first proposed with the USGS Tetracorder (Clark et al., 2003) and MICA (Kokaly et al. 2012; Material Identification and Characterization Algorithm) algorithms in an operational and scalable way.

This is the peer-reviewed, final accepted version for American Mineralogist, published by the Mineralogical Society of America.
The published version is subject to change. Cite as Authors (Year) Title. American Mineralogist, in press.
DOI: https://doi.org/10.2138/am-2021-7656. http://www.minsocam.org/

Both algorithms use spectral reference libraries and manual expert- and user-defined feature databases (Clark et al., 2007) to characterize surface material from an image spectroscopy dataset. This work uses the EnMAP Geological Mapper (EnGeoMAP) in its second version (Mielke et al., 2016). The main difference to the aforementioned algorithms is the automated definition of characteristic absorption bands in both the unknown image spectroscopy dataset and the reference library, assuming no *a priori* expert knowledge on the shape and position of the characteristic absorption features. The absorption band retrieval is carried out using the geometric hull absorption band retrieval algorithm (Mielke et al., 2015) via continuum removal (Clark et al., 1987).

## 4. Results

### *4.1. VNIR and mid-IR spectral measurements on rock powders and fractions*

VNIR reflectance spectra measured under ambient conditions from 0.35 to 2.5 μm of the rock powders and coarse grained material indicate the presence of alteration minerals (Figure 3). Spectra of the KM-27 and KM-Dun samples (Figure 3b) have features consistent with serpentine including strong, narrow bands at 1.39 and 2.33 μm (e.g. King and Clark, 1989; Bishop et al., 2008). Additional features due to serpentine are present in spectra of these samples near 1.91, 1.98, 2.11, and 2.45 μm (Figure 3d). Spectra of the KM-spin 4 and KM-spin 18 samples exhibit similar spectral features, although they are much weaker, indicating some serpentine is present. Spectra of the THS-4 samples (Figure 3a) have bands near 1.39, 1.91, 1.98, 2.11, 2.25, 2.32 and 2.38 μm that are consistent with a mixture of Mg-rich chlorite and serpentine. Spectra of the KV1 samples (Figure 3a) have bands near 1.41 and 2.21 μm that are consistent with Al-OH in montmorillonite or mica, as well as a broad water band with a minimum at 1.91 μm consistent with smectite minerals (e.g. Bishop et al., 2008). Variance in the shape of the Fe bands near 0.65-0.75, 0.88-0.93, and 1.03-1.13 μm, the shape of the water band near 1.9-2.0 μm and the position of the OH bands near 2.25-2.5 μm are attributed to changes in the Fe/Mg-rich phyllosilicates. Spectra of several Fe/Mg-clays and olivine (forsterite) are included in Figure 3d for comparison.

VNIR spectra of the coarse-grained samples measured under a $H_2O$-scrubbed environment from 0.3-4 μm are shown in Figure 4a,c. These data show shifts in the OH and $H_2O$ stretching vibrations near 1.4, 1.9, 2.2-2.3, and 2.7-3 μm. KV1 has features consistent with serpentine and quartz, while the THS-4 and KM-Dun-b spectra are darker and likely contain some basalt in addition to the chlorite and serpentine. The KM-27, KM-spin-4, and KM-spin-18 spectra are dominated by a downward slope characteristic of coatings or mixtures of grain size (e.g., Bishop, 2019).

Mid-IR reflectance spectra of the coarse-grained samples are shown in Figure 4b, d. The reflectance features near 1000-1200 $cm^{-1}$ and from ~350-650 $cm^{-1}$ are characteristic of silicate minerals (e.g. Salisbury et al., 1991; Lane and Bishop, 2019). The KV1 spectrum again appears to have the strongest spectral component due to quartz based on features near 1100-1200 $cm^{-1}$ (Figure 4b). The spectra of THS-4 and KM-Dun-b exhibit a basaltic type shape with additional features consistent with chlorite (Figure 4b). The KM-spin 4 spectrum contains features due to serpentine and chlorite near 1100, 1050, 870, 650, 500-470 $cm^{-1}$, while the KM-27 and KM-spin 18 spectra include features due to serpentine and chlorite, but also contain a broader band near 950-1000 $cm^{-1}$ that could be due to forsteritic olivine and a shoulder near 550 $cm^{-1}$consistent with magnetite (Figure 4d).

Mid-IR emission spectra from ~600-1800 $cm^{-1}$ of the samples are presented in Figure 5. For KV1 spectra were recorded for the slab, coarse grains and powder (Figure 5a). The KV1 slab spectrum includes some features consistent with a mixture of basalt and chlorite, but spectra of the particulate samples are more consistent with a mixture containing quartz (Figure 5b). The quartz grains in this sample are apparently more dominant in the particulate samples. Emission spectra of quartz include features due to Si-O stretching vibrations near 1100-1200 $cm^{-1}$ and bending vibrations near 500 $cm^{-1}$ (e.g. Wenrich and Christensen, 1996; Christensen et al., 2000; Land and Bishop, 2019). Basalt emission spectra in this region exhibit a broader band in the silicate stretching region that has been important in modeling the spectra of Mars (e.g. Christensen et al., 2001). Spectra of plagioclase (albite) and hornblende are also shown for comparison as they were found in petrologic analyses and could be present at lower abundances based on the emission spectra. The THS-4 emission spectra are dominated by features due to the chlorite mineral chamosite (Figure 5b) as also observed in the VNIR spectra. The chlorite-type

bands near 950, 1030, and 1070 $cm^{-1}$ are observed in both grain sizes of this sample, although the water band near1600 $cm^{-1}$ is more pronounced in the spectrum of the fine-grained sample, as expected. Emission spectra of KM-27 and KM-Dun-b (Figure 5c) include features consistent with serpentine and chamosite, but also contain a broader emission features spanning 900-1200 $cm^{-1}$ that is consistent with basalt. Emission spectra of KM-spin-4 and KM-spin-18 (Figure 5d) are even more characteristic of basalt, but could have smaller components of serpentine or olivine, as found in the petrologic analyses.

### *4.2. Spectral imaging of rock slabs*

False color composite images of the rock slabs are shown in Figure 6a,b and point spectra of locations marked on Figure 6a,b are shown in Figure 6f,g together with mineral reference spectra from the United States Geological Survey (USGS) digital spectral library (Clark et al., 2007). The extracted characteristic absorption bands of the unknown image pixel spectrum and the reference library standards are compared via a weighted fitting technique similar to the Tetracorder (Clark et al., 2003) and MICA (Kokaly et al. 2012) algorithms. Figure 6c,d,e shows a best weighted fit material map using sensor specific thresholds, which are lower than the user defined threshold values considering the high Signal to Noise Performance (SNR) of the HySpex system (Baarstad et al., 2005).

Samples such as KMK-6 and KR1 are too dark (low overall albedo) to be analyzed with reflectance values below the dark cellular-rubber background, as shown in Figure 6f. The hyperspectral scanning of the samples indicates the presence of clay minerals, in particular chlorite and serpentine. The reflectance spectra of samples KM-Dun and THS-4 indicate the presence of both chlorite and serpentine, consistent with the petrographic identification from thin section microscopy (see Figure 2). VNIR spectral imaging of sample KM-2c revealed the presence of antigorite veins, also consistent with the petrographic observations (Figure 2c). Collectively, the HySpex VNIR imaging method tested here succeeded in mapping chlorite and serpentine clay mineralogy identified in our samples through petrographic thin-section analyses, and bulk VNIR and mid-IR spectral measurements.

379 Spectra of a few surface spots from the HySpex imaging spectrometer are compared with
380 bulk spectra of the crushed samples in Figure 7. These data illustrate how the bulk spectra
381 contain features present in one or two spot spectra that are focused on individual mineral grains
382 in the rock. For example, the surface spot measured on rock slab KM 2C contains features due to
383 chlorite that are also found in the spectra of the THS-4 bulk grains sample. The HC3A surface
384 spot spectrum contains a broad Fe band near 0.9-1.2 μm that is consistent with olivine, bands
385 near 2.0, 2.25 and 2.35 μm that are consistent with chamosite, and a band at 2.20 μm due to Al-
386 OH in phyllosilicates. Spectra of the KV1 surface spot and KV1 bulk grains also contain
387 phyllosilicate OH features from 2.2 to 2.35 μm, but show variations in the abundance of the
388 chamosite and Al-smectite. The KM-Dun spectra exhibit basalt-type signatures and the basalt
389 band is more clearly defined in the surface spot spectrum. A small shift in the wavelength of the
390 OH combination band near 2.33-2.35 μm represents changes in the Fe/Mg abundance in the
391 chlorite measured by each technique.

392

393 **5. Discussion**

394 Based on orbital data, a very wide range of aqueous environments of Noachian age has been
395 recognized on Mars, and their occurrence implies that hydrothermal sub-surface alteration of
396 mafic-ultramafic rocks was widespread during the Noachian Period on ancient Mars (Wray et al.,
397 2009; Bishop et al., 2013a, 2018). It is likely that some of the low-temperature clay minerals
398 observed on Mars are due to hydrothermal processes, particularly those associated with large
399 impact craters. Smectite, kaolinite, and illite are common clay minerals on Mars that form at low
400 temperatures below ~100 $^{o}$C. However, moderate to higher temperature clay minerals (~100-400
401 °C) such as serpentine, chlorite, and talc have been confirmed in Leighton Crater and other sites
402 using hyperspectral analysis in crater ejecta, knobby terrains, or as part of discontinuous layers in
403 craters or valley walls of the Nili Fossae region (Amador et al., 2018; Brown et al., 2020).
404 Furthermore, olivine (precursor to serpentine) fractured rock units have been identified in deep
405 regions of craters in the Nili Fossae region (e.g. Bramble et al., 2017) of similar age to early
406 Archean rocks on Earth and serpentine has commonly been found as a possible higher
407 temperature mineral in other regions of Mars (e.g. Ehlmann et al., 2010). Amador et al., (2018)
408 have argued that serpentinization processes were pervasive in the early part of Mars' history as it

409 was more geologically active then. Hence early Earth and early Mars may have had similar
410 serpentinization processes in their early geological histories.

411 Even though not all alteration processes would have been the same on early Earth and
412 Mars, the current study proposes that some subsurface mafic-ultramafic hydrothermal
413 environments on ancient Mars and early Archean Earth may have been similar. In this context,
414 the rock sequences of the Paleoarchean Barberton greenstone belt of South Africa provide
415 unique martian analogues as these rocks are exceptionally well-preserved and record early Earth
416 (and perhaps martian-type) subsurface hydrothermal/alteration processes. *In-situ* exploration by
417 rovers, remote sensing studies, and meteorite evidence has indicated the presence of altered
418 gabbros, olivine-/pyroxene-bearing metabasalts and possible serpentinites on Mars (e.g., Ehlman
419 and Edwards, 2014; Ruff et al., 2019; Hamilton et al., 2019; Murchie et al., 2019; McSween,
420 2015). We present selected 3.5 to 3.3 billion-year-old Archean greenstone belt analogue samples
421 that include altered tholeiitic metabasalts and serpentinized ultramafic rocks. Spectroscopic
422 measurements were conducted on different scales, namely bulk analyses on rock fragments and
423 rock powders, and microscale analyses on rock slabs by HySpex *in-situ* analysis. VNIR
424 reflectance, mid-IR emission and VNIR spectral imaging have successfully identified serpentine
425 and chlorite alteration mineralogy irrespective of scale or material form. The petrography and
426 mineralogy of the samples were analyzed in terms of relic igneous phases and clay mineral
427 alteration and are in good agreement with spectral identification of minerals in the samples. We
428 expanded past studies by acquiring VNIR reflectance and mid-IR emission spectra on these early
429 Archean samples for comparison with orbital spectral data of Mars.

430 The HySpex instrument hyperspectral data used to 'map' the mineralogy of the rock
431 samples has proven to be useful in mineral identification and the results compare well with bulk
432 spectroscopic analyses. This technique has potential to provide useful information for both
433 terrestrial studies and studies seeking to understand hydrothermal alteration of rocks from current
434 or future Mars missions. The power of imaging spectroscopy is that it coordinates textural and
435 spatial information with mineralogy, information that is not gained from bulk analysis of rock
436 powders or rock chips. This spatial and textural-related data are needed to demonstrate that a
437 clay-bearing deposit on Mars may be hydrothermal in origin and also that a terrestrial deposit
438 may indeed be a useful Mars analogue. These kinds of analyses will be particularly useful in

preparing for the micromega analyses to be collected by the ExoMars rover (Bibring et al., 2017). The relationships between alteration phases, primary igneous minerals and textural characteristics are critical for piecing together the process history of metamorphosed terrestrial and extra-terrestrial mafic and ultramafic rocks. In theory, *in situ* imaging spectroscopy of relevant rock surfaces has the power to aid in this type of direct comparative study. A HySpex-type instrument such as micromega attached to a Mars rover could also provide useful *in situ* scans of rock texture, mineralogy, and the alteration processes producing clay minerals.

## 6. Implications

The Archean Barberton greenstone belt rocks hold significant potential for future petrological analogue studies for Mars. Remote sensing hyperspectral studies on Mars have revealed evidence for hydrothermal activity involving, not only chloritization, but also carbonate formation in altered mafic-ultramafic rocks (e.g., Viviano et al. 2013; Ehlmann and Edwards, 2014; Lane et al., 1997; Hamilton et al., 2019; Brown et al., 2020), sulphates (Bishop et al., 2013a) and hematite on Mars (Christensen et al., 2000, 2001; Lane et al., 2002). A number of early Archean rocks from the Barberton greenstone belt could serve as hyperspectral petrological analogues for martian environments in future analogue studies: Banded Iron Formations (BIF) for hematite and magnetite layers; hydrothermal and sedimentary barite units for sulphate analogues; as well as carbonitized and silicified mafic-ultramafic rocks for siderite, dolomite and calcite hyperspectral studies. Silicified metabasalts and serpentinites of the Barberton greenstone belt may also contribute to understanding acid leaching processes on Mars (c.f. Yant et al., 2016). The upcoming Mars2020 rover analyses of Jezero crater will investigate phyllosilicate and carbonate-bearing outcrops in delta sediments, as well as basaltic bedrock containing olivine, chlorite, and serpentine (e.g., Goudge et al. 2017, Bramble et al., 2017; Amador et al., 2018; Brown et al., 2020). If chlorite- and serpentine-bearing rocks are encountered by Mars2020, the rock textures and spectral analyses in this study will provide ground truth for understanding the potential formation conditions for those rocks.

## Figures

***Figure 1.*** Simplified geological map of the Barberton greenstone belt (BGB). (a-b) Geographical location of the BGB on the boundary between South Africa and Swaziland. (c ). Geological map with U-Pb age constraints of various rock types of the Onverwacht Group of the Barberton Supergroup (see Grosch et al., 2011 and references therein). (d – h) Various field outcrops showing altered serpentinized ultramafic rocks and metabasalts as potential analogue sites for hydrothermal alteration of crust on Mars.

***Figure 2.*** Petrographic images of relevant mafic and ultramafic rock types with associated low-temperature alteration assemblages (white scale bar is 200 μm). (a) KM-Dun = chloritized metadunite, (b) serpentinized olivine spinifex komatiite, (c) KM-2c = serpentinized komatiite with serpentine extensional veins (d) KM-K6 = serpentinized peridotitic komatiite with minor alteration veins (e) = HC3 chlorite – epidote – quartz assemblage in metabasaltic pillow lava chilled margin (f) altered komatiitic basalt with Cr- chlorite, serpentine and accessory opaques.

***Figure 3.*** VNIR reflectance spectra from 0.35 to 2.5 μm measured with the ASD spectrometer under ambient conditions. (a) KV1 and THS-4 spectra, (b) KM-27 and Km-Dun-b spectra, (c) KM-spin 4 and KM-spin 18 spectra, (d) fine-grained BGB samples compared with minerals from the Bishop library (e.g. Bishop, 2019) and synthetic olivine (Fo90) from Isaacson et al. (2014). Spectral features due to electronic or vibrational absorptions are marked on the plots to facilitate comparison of the BGB samples with each other and their mineral components.

***Figure 4.***

Reflectance spectra across the VNIR and mid-IR range measured under an $H_2O$- and $CO_2$-purged environment. Spectra of the coarse-grained samples KV1, THS-4, and ZKM-Dun-b are shown in (a) from 0.3-4 μm as a function of wavelength and (b) from 1400 to 300 $cm^{-1}$ as a function of wavenumber, while spectra of KM-27, KM-spin-4, and KM-spin-18 are shown in (c) and (d). Reflectance spectra of basalt and selected minerals (Bishop, 2019) are provided for comparison. Spectra of the clay minerals chamosite (Fe-rich chlorite, solid line), clinochlore (Mg-rich chlorite, dotted line), lizardite (serpentine, solid line), chrysotile (serpentine, dotted line) and montmorillonite SAz-1 (Al-rich smectite) are from Bishop et al. (2008), and the basalt spectrum of sample G2 from Bishop et al. (2002) is described in Harloff et al. (2001). Vertical lines mark features due to minerals in the spectra.

***Figure 5.***

Mid-IR emission spectra of BGB samples (a) KV1, (b) THS-4, (c) KM-Dun-b and KM-27, and (d) KM-spin-4 and KM-spin-18. Spectra are shown for multiple sample textures for samples KV1 and THS-4 to illustrate the influence of grain size and surface type on the spectra. Emission spectra of selected minerals and basalt are shown for comparison. Emission spectra of the chamosite (Fe-rich chlorite) is from Bishop et al. (2008), the basalt spectrum is sample G2 from Bishop et al. (2002) that is described in Harloff et al. (2001), the serpentine, hornblende and forsterite are from Lane and Bishop (2019), and the quartz and albite spectra are from the ASU library (Christensen et al., 2000). Vertical lines mark features in the BGB spectra associated with the rock and mineral spectra.

***Figure 6.*** VNIR spectral imaging of rock slabs KMK-6, KD-Pyrox, KR1, KM-2C, THS4, KM-DUN and HC3A. (a) color maps of the rock slabs using R: 640 nm, G: 549 nm, B: 458 nm, (b) color maps of the rock slabs using R: 2222 nm, G: 890 nm, B: 553 nm, (c) maps of correlation values, (d) maps of the best fit plus gradient, (e) maps of the best fit, (f) VNIR spectra collected from regions on the rock slabs marked in (a) and (b) that were selected to highlight the observed clay mineralogy in the samples, and (g) lab spectra of minerals from the USGS spectral library for comparison.

***Figure 7.*** Spectra of a few surface spots from the HySpex imaging spectrometer compared in the same diagram with bulk spectra of the selected crushed samples.

## Table Captions

***Table 1.*** Whole rock compositions in wt.% element oxides of a typical BGB metabasalt compared to altered metabasalts on Mars.

***Table 2.*** List of samples in the study and their locations in the BGB stratigraphy. For further information on rock age see Grosch et al., (2011)

***Table 3.*** List of samples and analytical technique

## Acknowledgements

The authors are grateful for the assistance of T. Hiroi in measuring reflectance spectra at the NASA-supported RELAB facility at Brown University and to M. Lane for helpful comments during review. The authors also appreciate the use of mineral spectra from the Arizona State University (ASU) Mars Space Flight Facility: https://speclib.asu.edu/, and the United States Geological Survey (USGS) spectroscopy lab: https://www.usgs.gov/labs/spec-lab/capabilities/spectral-library.

## References

Amador, E.S., Bandfield J.L., and Thomas N.H. (2018) A search for minerals associated with serpentinization across Mars using CRISM spectral data. Icarus, 311, 113-134.

Baarstad, I.; Løke, T.; Kaspersen, P. (2005) ASI–A new airborne hyperspectral imager. In Proceedings of the 4th EARSeL Workshop on Imaging Spectroscopy–New Quality in Environmental Studies. Warsaw, Poland.

Banerjee, N.R., Simonetti, A., Furnes, H., Staudigel, H., Muehlenbachs, K., Heaman, L., and Van Kranendonk, M.J. (2007) Direct dating of Archean microbial ichnofossils. Geology 35, 487–490.

Bibring, J.-P., Hamm V., Pilorget C., Vago J.L., and MicrOmega T. (2017) The MicrOmega Investigation Onboard ExoMars. Astrobiology, 17, 621-626.

Bishop, J.L. (2019) Visible and near-infrared reflectance spectroscopy of geologic materials. In J. L. Bishop, J. F. Bell III, and J. E. Moersch, Eds., Remote Compositional Analysis: Techniques for Understanding Spectroscopy, Mineralogy, and Geochemistry of Planetary Surfaces, 68-101, Chapter 4, Cambridge University Press. Cambridge, UK.

Bishop, J.L., Schiffman P., and Southard R.J. (2002) Geochemical and mineralogical analyses of palagonitic tuffs and altered rinds of pillow lavas on Iceland and applications to Mars. In J. L. Smellie and M. G. Chapman, Eds., Volcano-Ice Interactions on Earth and Mars, 371-392. Geological Society, Special Publication No.202. London.

562 Bishop, J.L., Murad E., Lane M.D., and Mancinelli R.L. (2004) Multiple techniques for mineral
563 identification on Mars: A study of hydrothermal rocks as potential analogues for
564 astrobiology sites on Mars. Icarus, 169, 331-323.

565 Bishop, J.L., Schiffman P., Murad E., Dyar M.D., Drief A., and Lane M.D. (2007)
566 Characterization of Alteration Products in Tephra from Haleakala, Maui: A Visible-
567 Infrared Spectroscopy, Mössbauer Spectroscopy, XRD, EPMA and TEM Study. Clays
568 and Clay Minerals, 55, 1-17.

569 Bishop, J.L., Lane M.D., Dyar M.D., and Brown A.J. (2008) Reflectance and emission
570 spectroscopy study of four groups of phyllosilicates: Smectites, kaolinite-serpentines,
571 chlorites and micas. Clay Minerals, 43, 35-54.

572 Bishop, J.L., Tirsch, D., Tornabene, L.L., Jaumann, R., McEwen, A.S., McGuire, P.C., Ody, A.,
573 Poulet, F., Clark, R.N., Parente, M., McKeown, N.K., Mustard, J.F., Murchie, S.L.,
574 Voigt, J., Aydin, Z., Bamberg, M., Petau, A., Michael, G., Seelos, F.P., Hash, C.D.,
575 Swayze, G.A., and Neukum, G. (2013) Mineralogy and morphology of geological units at
576 Libya Montes, Mars: ancient aqueously derived outcrops, mafic flows, fluvial features,
577 and impacts. Journal of Geophysical Research: Planets, 118, 487–513.

578 Bishop, J.L., Fairén A.G., Michalski J.R., Gago-Duport L., Baker L.L., Velbel M.A., Gross C.,
579 and Rampe E.B. (2018) Surface clay formation during short-term warmer and wetter
580 conditions on a largely cold ancient Mars. Nature Astronomy, 2, 206-213.

581 Bost, N., Westall, F., Ramboz, C., Fouchera, F., Pullan, D., Meunier, A., Petit, S., Fleischer, I.,
582 Klingelhöfer, G., and Vago, J.L. (2013) Missions to Mars: characterisation of Mars
583 analogue rocks for the International Space Analogue Rockstore (ISAR). Planet and Space
584 Science, 82–83, 113–127.

585 Bramble, M.S., Mustard J.F., and Salvatore M.R. (2017) The geological history of Northeast
586 Syrtis Major, Mars. Icarus, 293, 66-93.

587 Bridges, J.C., Schwenzer S.P., Leveille R., Westall F., Wiens R.C., Mangold N., Bristow T.,
588 Edwards P., and Berger G. (2015) Diagenesis and clay mineral formation at Gale Crater,
589 Mars. Journal of Geophysical Research: Planets, 120, 1-19.

590 Bristow, T.F., Bish D.L., Vaniman D.T., Morris R.V., Blake D.F., Grotzinger J.P., Rampe E.B.,
591 Crisp J.A., Achilles C.N., Ming D.W., Ehlmann B.L., King P.L., Bridges J.C.,
592 Eigenbrode J.L., Sumner D.Y., Chipera S.J., Moorokian J.M., Treiman A.H., Morrison
593 S.M., Downs R.T., Farmer J.D., Marais D.D., Sarrazin P., Floyd M.M., Mischna M.A.,
594 and McAdam A.C. (2015) The origin and implications of clay minerals from Yellowknife
595 Bay, Gale crater, Mars. American Mineralogist, 100, 824-836.

596 Brown, A.J., Walter, M.R. and Cudahy, T.J. (2007) Hyperspectral imaging spectroscopy of a
597 Mars analogue environment at the North Pole Dome, Pilbara Craton, Western Australia,
598 Australian Journal of Earth Sciences, 52:3, 353-364.

599 Brown, A.J., Walter, M.R. and Cudahy, T.J. (2004) Short-wave infrared reflectance
600 investigation of sites of paleobiological interest: applications for Mars exploration.
601 Astrobiology, 4(3), 359-376.

602 Brown, A.J., Viviano C.E., and Goudge T.A. (2020) Olivine-Carbonate Mineralogy of the Jezero
603 Crater Region. Journal of Geophysical Research: Planets, 125, e2019JE006011.

604 Christensen, P.R., Bandfield J.L., Hamilton V.E., Lane M.D., Piatek J.L., Ruff S.W., and
605 Stefanov W.L. (2000) A thermal emission spectral library of rock-forming minerals.
606 Journal of Geophysical Research, 105, 9735-9739.

607 Christensen, P.R., Bandfield J.L., Hamilton V.E., Ruff S.W., Kieffer H.H., Titus T.N., Malin
608 M.C., Morris R.V., Lane M.D., Clark R.L., Jakosky B.M., Mellon M.T., Pearl J.C.,
609 Conrath B.J., Smith M.D., Clancy R.T., Kuzmin R.O., Roush T., Mehall G.L., Gorelick
610 N., Bender K., Murray K., Dason S., Greene E., Silverman S., and Greenfield M. (2001)
611 Mars Global Surveyor Thermal Emission Spectrometer experiment: Investigation
612 description and surface science results. Journal of Geophysical Research, 106, 23, 823–
613 23,871.

614 Christensen, P. R., Mehall, G. L., Silverman, S. H., Anwar, S., Cannon, G., Gorelick, N., Kheen,
615 R., Tourville, T., Bates, D., Ferry, S. and Fortuna, T. (2003) Miniature Thermal Emission
616 Spectrometer for the Mars Exploration Rovers, Journal of Geophysical Research, 108
617 (E12), 8064.

Clark, R. N.; Swayze, G. A.; Wise, R., Livo, E., Hoefen, T. M., Kokaly, R. F., Sutley, S. J. (2007) USGS digital spectral library splib06a; Geological Survey (U.S.) Clark, Ed.; U.S. Geological Survey data series; Rev. Sept. 20, (2007) U.S. Geological Survey: Denver, CO.

Clark, R. N. (2003) Imaging spectroscopy: Earth and planetary remote sensing with the USGS Tetracorder and expert systems. Journal of Geophysical Research, 108 (E12).

Clark, R. N., King, T. V. V. and Gorelick, N. (1987) Automatic continuum analysis of reflectance spectra. Proceedings of the 3rd Airborne Imaging Spectrometer Data Analysis Workshop Passadena CA, 138–142.

Cockell, C. S. (2006) The origin and emergence of life under impact bombardment. Philosophical Transactions of the Royal Society of London. Series B, Biological Sciences, 361, 1845–1856.

Craddock, R.A. and Howard A.D. (2002) The case for rainfall on a warm, wet early Mars. Journal of Geophysical Research: Planets, 107, 21-1-21-36.

Cuadros, J., Michalski J.R., Dekov V., Bishop J., Fiore S., and Dyar M.D. (2013) Crystal-chemistry of interstratified Mg/Fe-clay minerals from seafloor hydrothermal sites. Chemical Geology, 360–361, 142-158.

Dann, J.C. (2000) The 3.5 Ga Komati Formation, Barberton Greenstone Belt, South Africa, Part I: New maps and magmatic architecture. South African Journal of Geology, 103, 47-68.

Dalton, J. B., Bove, D. J., Mladinich, C. S., Rockwell, B. W. (2004) Identification of spectrally similar materials using the USGS Tetracorder algorithm: the calcite–epidote–chlorite problem. Remote Sensing Environments, 89, 455–466.

Drabon, N., Heubeck, C.E., and Lowe, D. (2019). Evolution of an Archean fan delta and its implications for the initiation of uplift and deformation in the Barberton greenstone belt, South Africa. Journal of Sedimentary Research, 89 (9), 849–874.

Edwards, K.J., Wheat, C.G., and Sylvan, J.B. (2011) Under the sea: Microbial life in volcanic oceanic crust. Nature Reviews Microbiology, 9, 703-712

Ehlmann, B.L., Mustard J.F., Swayze G.A., Clark R.N., Bishop J.L., Poulet F., Marais D.J.D., Roach L.H., Milliken R.E., Wray J.J., Barnouin-Jha O., and Murchie S.L. (2009) Identification of hydrated silicate minerals on Mars using MRO-CRISM: Geologic context near Nili Fossae and implications for aqueous alteration. Journal of Geophysical Research, 114 (E2), doi:10.1029/2009JE003339.

Ehlmann, B.L., Mustard J.F., and Murchie S.L. (2010) Geologic setting of serpentine deposits on Mars. Geophys. Res. Lett., 37(6), L06201, doi:10.1029/2010GL042596.

Ehlmann, B.L., Mustard, J.F., Murchie, S.L., Bibring, J.P., Meunier, A., Fraeman, A.A., and Langevin, Y. (2011a) Subsurface water and clay mineral formation during the early history of Mars. Nature, 479, 53–60.

Ehlmann, B.L., Mustard, J.F., Clark, R.N., Swayze, G.A., and Murchie, S.L. (2011b) Evidence for low-grade metamorphism, diagenesis, and hydrothermal alteration on Mars from phyllosilicate mineral assemblages. Clays and Clay Minerals, 59, 359–377.

Ehlmann, B.L., Mustard, J.F., Murchie, S.L., Bibring, J.-P., Meunier, A., Fraeman, A.A., and Langevin, Y. (2013) Geochemical consequences of widespread clay mineral formation in Mars' ancient crust. Space Science Reviews, 174, 329–364.

Ehlmann, B.L. and Edwards C.S. (2014) Mineralogy of the Martian Surface. Annual Review of Earth and Planetary Sciences, 42, 291-315.

Fisk, M.R., Giovannoni, S.J., and Thorseth, I.H. (1998) Alteration of oceanic volcanic glass: textural evidence of microbial activity. Science, 281, 978–980.

Furnes, H., Staudigel, H., Thorseth, I.H., Torsvik, T., Muehlenbachs, K., and Tumyr, O. (2001) Bioalteration of basaltic glass in the oceanic crust. Geochemistry, Geophysics, Geosystems 2, GC000170.

Furnes, H., Banerjee, NR, Muehlenbachs, K., Staudigel, H., and de Wit, M.J. (2004) Early life recorded in Archean pillow lavas. Science, 304, 578–581.

Furnes, H., Banerjee, N.R., Staudigel, H., Muehlenbachs, K., McLoughlin, N., de Wit, M., and Van Kranendonk, M., (2007) Comparing petrographic signatures of bioalteration in recent to Mesoarchean pillow lavas: Tracing subsurface life in oceanic igneous rocks. Precambrian Research, 158, 156–176.

674 Furnes, H., de Wit, M.J., Robins, B., and Sandståd, N.R. (2011) Volcanic evolution of the upper
675 Onverwacht Suite, Barberton Greenstone Belt, South Africa. Precambrian Research, 186,
676 28-50.

677 Goudge, T.A., Milliken R.E., Head J.W., Mustard J.F., and Fassett C.I. (2017) Sedimentological
678 evidence for a deltaic origin of the western fan deposit in Jezero crater, Mars and
679 implications for future exploration. Earth and Planetary Science Letters, 458, 357-365.

680 Grosch, E. G., McLoughlin, N., deWit, M. J. & Furnes, H. (2009) Deciphering Earth's deep
681 history: drilling in Africa's oldest greenstone belt. EOS Transactions, American
682 Geophysical Union, 90, 350-351.

683 Grosch, E. G., Kosler, J., McLoughlin, N., Drost, K., Slama, J. & Pedersen, R. B. (2011)
684 Paleoarchean detrital zircon ages from the earliest tectonic basin in the Barberton
685 Greenstone Belt, Kaapvaal craton, South Africa. Precambrian Research, 191, 85-99.

686 Grosch, E.G., Vidal, O., Abu-Alam, T., and McLoughlin, N. (2012) PT-constraints on the
687 metamorphic evolution of the Paleoarchean Kromberg type-section, Barberton
688 greenstone belt, South Africa. Journal of Petrology, 53, 513–545.

689 Grosch, E.G. and Mcloughlin, N. (2014) Reassessing the biogenicity of Earth's oldest trace fossil
690 with implications for biosignatures in the search for early life. Proceedings of the
691 National Academy of Sciences, 111, 8380-8385

692 Grosch, E.G., and Hazen, R. M. (2015) Microbes, Mineral Evolution, and the Rise of
693 Microcontinents—Origin and Coevolution of Life with Early Earth, Astrobiology.
694 15(10), 922-939.

695 Hamilton, V.E. and Christensen P.R. (2005) Evidence for extensive, olivine-rich bedrock on
696 Mars. Geology, 33, 433-436.

697 Hamilton, V.E., Morris R.V., Gruener J.E., and Mertzman S.A. (2008) Visible, near-infrared,
698 and middle infrared spectroscopy of altered basaltic tephras: Spectral signatures of
699 phyllosilicates, sulfates, and other aqueous alteration products with application to the
700 mineralogy of the Columbia Hills of Gusev Crater, Mars. Journal of Geophysical
701 Research: Planets, 113(E12), doi: 10.1029/2007JE003049.

Hamilton, V.E., Christensen P.R., Bandfield J.L., Rogers A.D., Edwards C.S., and Ruff S.W. (2019) Thermal infrared spectral analyses of Mars from orbit using the Thermal Emission Spectrometer and Thermal Emission Imaging System. In J. L. Bishop, J. E. Moersch, and J. F. Bell III, Eds., Remote Compositional Analysis: Techniques for Understanding Spectroscopy, Mineralogy, and Geochemistry of Planetary Surfaces, 484-498. Chapter 24, Cambridge University Press. Cambridge, UK.

Hunt, J. M. and Turner, D. S. (1953) Determination of Mineral Constituents of Rocks by Infrared Spectroscopy. Analytical Chemistry, 25, 1169–1174.

Hunt, G. R. and Ashley, R. P. (1979) Spectra of altered rocks in the visible and near infrared. Economic Geology, 74, 1613–1629.

Hoffman, A and Harris, C., (2008) Stratiform alteration zones in Barberton Greenstone belt: a window into subseafloor processes 3.5-3.3 Ga ago. Chemical Geology, 257, 224-242.

Hanor, J.S. and Duchac, K.C. (1990) Isovolumetric silicification of early Archean komatiites: geochemical mass balances and constraints on origin. Journal of Geology, 98, 863–877.

Isaacson, P.J., Klima R.L., Sunshine J.M., Cheek L.C., Pieters C.M., Hiroi T., Dyar M.D., Lane M.D. and Bishop J.L. (2014) Visible to near-infrared optical properties of pure synthetic olivine across the olivine solid solution. American Mineralogist, 99, 467-478.

Izawa M, Banerjee NR, Shervais JW, Flemming RL, Hetherington CJ, Muehlenbachs K, Schultz C, Das D, Hanan BB. (2019) Titanite mineralization of Microbial Bioalteration textures in Jurassic Volcanic Glass, Coast Range Ophiolite, California. Frontiers in Earth Science, 7, 315.

King, T.V.V. and Clark R.N. (1989) Spectral characteristics of chlorites and Mg-serpentines using high-resolution reflectance spectroscopy. Journal of Geophysical Research, 94, 13, 997-14, 008.

Kokaly, R. F. Spectroscopic remote sensing for material identification, vegetation characterization, and mapping. (2012) In Proceedings of the SPIE 8390, Algorithms and Technologies for Multispectral, Hyperspectral and Ultraspectral Imagery XVIII; Baltimore Marryland, Volume. 8390, pp. 839014–839014–12.

730 Lane M.D., and PR Christensen. (1997) Thermal infrared emission spectroscopy of anhydrous
731 carbonates, Journal of Geophysical Research: Planets 102 (E11), 25581-25592.

732 Lane, M.D. and Bishop J.L. (2019) Mid-infrared (thermal) emission and reflectance
733 spectroscopy. In J. L. Bishop, J. F. Bell III, and J. E. Moersch, Eds., Remote
734 Compositional Analysis: Techniques for Understanding Spectroscopy, Mineralogy, and
735 Geochemistry of Planetary Surfaces, 42-67, Chapter 3, Cambridge University Press.
736 Cambridge, UK.

737 Lane, M.D., Morris, R.V. Mertzman, S.A., Christensen, P.R. (2002) Evidence for platy hematite
738 grains in Sinus Meridiani, Mars. Journal of Geophysical Research: Planets 107 (E12).

739 Lowe, D. R., Byerly, G. R., & Kyte, F. T. (2014) Recently discovered 3.42–3.23 Ga impact
740 layers, Barberton Belt, South Africa: 3.8 Ga detrital zircons, Archean impact history, and
741 tectonic implications. Geology, 42(9), 747-750.

742 Lowe, D. R., Byerly, G. R., Kyte, F. T., Shukolyukov, A., Asaro, F., & Krull, A. (2003) Spherule
743 beds 3.47–3.24 billion years old in the Barberton Greenstone Belt, South Africa: a record
744 of large meteorite impacts and their influence on early crustal and biological evolution.
745 Astrobiology, 3(1), 7-48.

746 Marzo, G.A., Davila A.F., Tornabene L.L., Dohm J.M., Fairén A.G., Gross C., Kneissl T.,
747 Bishop J.L., Roush T.L. and McKay C.P. (2010) Evidence for Hesperian impact-induced
748 hydrothermalism on Mars. Icarus, 208, 667-683.

749 Maturilli, A., Helbert J., and Arnold G. (2019) The newly improved set-up at the Planetary
750 Spectroscopy Laboratory (PSL). Proc. SPIE 11128. Infrared Remote Sensing and
751 Instrumentation XXVII111280T.

752 McSween, H.Y. (2015) Petrology on Mars. American Mineralogist, 100, 2380-2395.

753 Michalski, J.R., Kraft M.D., Sharp T.G., and Christensen P.R. (2006) Effects of chemical
754 weathering on infrared spectra of Columbia River Basalt and spectral interpretations of
755 martian alteration. Earth and Planetary Science Letters, 248, 822-829.

756 Michalski, J.R., Cuadros, J., Niles, P.B., Parnell, J., Rogers, A.D., and Wright, S.P. (2013)
757 Groundwater activity on Mars and implications for a deep biosphere. Nature Geoscience
758 6, 133–138.

759 Michalski, J.R., Cuadros J., Bishop J.L., Darby Dyar M., Dekov V., and Fiore S. (2015)
760 Constraints on the crystal-chemistry of Fe/Mg-rich smectitic clays on Mars and links to
761 global alteration trends. Earth and Planetary Science Letters, 427, 215-225.

762 Michalski, J.R., Glotch T.D., Rogers A.D., Niles P.B., Cuadros J., Ashley J.W., and Johnson S.S.
763 (2019) The Geology and Astrobiology of McLaughlin Crater, Mars: An Ancient
764 Lacustrine Basin Containing Turbidites, Mudstones, and Serpentinites. Journal of
765 Geophysical Research: Planets, 124, 910-940.

766 Murchie, S.L., Bibring J.P., Arvidson R.E., Bishop J.L., Carter J., Ehlmann B.L., Langevin Y.,
767 Mustard J.F., Poulet F., Riu L., Seelos K.D., and Viviano C.E. (2019) Visible to short-
768 wave Infrared spectral analyses of Mars from orbit using CRISM and OMEGA. In J. L.
769 Bishop, J. E. Moersch, and J. F. Bell III, Eds., Remote Compositional Analysis:
770 Techniques for Understanding Spectroscopy, Mineralogy, and Geochemistry of Planetary
771 Surfaces, 453-483, Chapter 23, Cambridge University Press. Cambridge, UK.

772 Mustard, J.F., Poulet F., Gendrin A., Bibring J.-., P., Langevin Y., Gondet B., Mangold N.,
773 Bellucci G., and Altieri F. (2005) Olivine and pyroxene diversity in the crust of Mars.
774 Science, 307, 1594-1597.

775 Mustard, J.F., Ehlmann B.L., Murchie S.L., Poulet F., Mangold N., Head J.W., Bibring J.-P., and
776 Roach L.H. (2009) Composition, morphology, and stratigraphy of Noachian crust around
777 the Isidis basin. Journal of Geophysical Research, 114 (E2), doi:10.1029/2009JE003349.

778 Michalski, J.R., Dobrea E.Z.N., Niles P.B., and Cuadros J. (2017) Ancient hydrothermal seafloor
779 deposits in Eridania basin on Mars. Nature Communications, 8, 15978.

780 Mielke, C.; Rogass, C.; Boesche, N.; Segl, K.; Altenberger, U. (2016) EnGeoMAP 2.0—
781 Automated Hyperspectral Mineral Identification for the German EnMAP Space Mission.
782 Remote Sensing, 8(2), 127.

783 Mielke, C.; Boesche, N. K.; Rogass, C.; Kaufmann, H.; Gauert, C. (2015) New geometric hull
784 continuum removal algorithm for automatic absorption band detection from
785 spectroscopic data. Remote Sensing Letters, 6, 97–105.

786 McLoughlin, N., Grosch, E.G., Kilburn, M., and Wacey, D. (2012) Sulfur isotope evidence for a
787 Paleoarchean subseafloor biosphere, Barberton, South Africa. Geology, 40, 1031–1034.

Mustard, J.F. and Tarnas J.D. (2017) Hydrogen Production from the Upper 15 km of Martian Crust via Serpentinzation: Implications for Habitability. Lunar and Planetary Science Conference. XLVIII, The Woodlands, TX, Abstract #2384.

Orcutt, B.N., Sylvan, J.B., Knab, N.J., and Edwards, K.J. (2011) Microbial ecology of the dark ocean above, at and below the seafloor. Microbiology and Molecular Biology Reviews, 75, 361-422.

Oze, C. and Sharma, M. (2005) Have olivine, will gas: serpentinization and the abiogenic production of methane on Mars. Geophysical Research Letters 32 (10), doi:10.1029/2005GL022691.

Philippot, P., Van Kranendonk, M., Van Zuilen, Lepot, K., Rividi, N., Teitler, Y., Thomazo, C., Blanc-Valleron, M., Rouchy, J., Grosch, E.G., de Wit, M.J. (2009) Drilling Archean hydrothermal and sedimentary settings of the Pilbara Craton, Western Australia and Barberton Belt, South Africa. Competus Rendus Palevol, 8, 649-663.

Ruff, S.W., Bandfield J.L., Christensen P.R., Glotch T.D., Hamilton V.E., and Rogers A.D. (2019) Thermal Infrared Remote Sensing of Mars from Rovers Using the Miniature Thermal Emission Spectrometer. In J. L. Bishop, J. F. Bell III, and J. E. Moersch, Eds., Remote Compositional Analysis: Techniques for Understanding Spectroscopy, Mineralogy, and Geochemistry of Planetary Surfaces, Chapter 25, Cambridge University Press. Cambridge, UK 499-512.

Salisbury, J.W., Walter L.S., Vergo N., and D'Aria D.M. (1991) Infrared (2.1-25 μm) Spectra of Minerals. 267 p. Johns Hopkins University Press, Baltimore.

Schiffman, P., Zierenberg R.A., Marks N., Bishop J.L., and Dyar M.D. (2006) Acid fog deposition at Kilauea Volcano: A possible mechanism for the formation of siliceous-sulfate rock coatings on Mars. Geology, 34, 921-924.

Staudigel, H., Furnes, H., McLoughlin, N., Banerjee, N.R., Connell, L.B., and Templeton, A. (2008) 3.5 billion years of glass bioalteration: Volcanic rocks as a basis for microbial life? Earth Science Reviews, 89(3-4), 156-176.

Squyres, S.W., Arvidson, R.E., Bell, J.F., III, Calef, F., III, Clark, B.C., Cohen, B.A., Crumpler, L.A., de Souza, P.A., Jr., Farrand, W.H., Gellert, R., Grant, J., Herkenhoff, K.E.,

817 Hurowitz, J.A., Johnson, J.R., Jolliff, B.L., Knoll, A.H., Li, R., McLennan, S.M., Ming,
818 D.W., Mittlefehldt, D.W., Parker, T.J., Paulsen, G., Rice, M.S., Ruff, S.W., Schroder, C.,
819 Yen, A.S., and Zacny, K. (2012) Ancient impact and aqueous processes at Endeavour
820 Crater, Mars. Science, 336, 570–576.

821 Thorseth, I.H., Torsvik, T., Furnes, H., and Muehlenbachs, K. (1995) Microbes play an
822 important role in the alteration of oceanic crust. Chemical Geology 126, 137–146.

823 Thorseth, I.H. (2011) Basalt (Glass, Endolith). In: Encyclopedia of Geobiology, Eds Reithner, J.,
824 and Thiel, V., Encyclopedia of Earth Sciences Series, pp103-111, Springer-Verlag.

825 Townsend, T. E. (1987) Discrimination of iron alteration minerals in visible and near-infrared
826 reflectance data. Journal of Geophysical Research Solid Earth, 92, 1441–1454.

827 Trowera, E.J. and Lowe, D.R. (2016). Sedimentology of the ~3.3 Ga upper Mendon Formation,
828 Barberton Greenstone Belt, South Africa. Precambrian Research, 281, 473-494.

829 Vedaldi, A., Fulkerson, B. (2008) VLFeat: An Open and Portable Library of Computer Vision
830 Algorithms. In Proceedings of the 18th ACM international conference on Multimedia, pp.
831 1469-1472.

832 Viljoen, M.J. and Viljoen, R.P. (1969b) The geology and geochemistry of the lower ultramafic
833 unit of the Onverwacht Group and a proposed new class of igneous rocks. Geological
834 Society of South Africa Special Publication, 2, 55-86.

835 Viviano, C. E., Moersch, J. E., & McSween, H. Y. (2013) Implications for early hydrothermal
836 environments on Mars through the spectral evidence for carbonation and chloritization
837 reactions in the Nili Fossae region. Journal of Geophysical Research: Planets, 118(9),
838 1858-1872.

839 Wenrich, M.L. and Christensen P.R. (1996) Optical constants of minerals derived from emission
840 spectrocopy: Application to quartz. Journal of Geophysical Research, 101, 15921-15931.

841 Wray, J.J., Murchie, S.L. Squyres, S.W., Seelos, F.P., Tornabene, L.L. (2009) Diverse aqueous
842 environments on ancient Mars revealed in the southern highlands. Geology, 37 (11),
843 1043-1046.

844 Yant, M., Young K.E., Rogers A.D., McAdam A.C., Bleacher J.E., Bishop J.L. and Mertzman
845 S.A. (2017) Visible, Near-Infrared and Mid-Infrared Spectral Characterization of
846 Hawaiian Fumarolic Alteration near Kilauea's December 1974 Flow: Implications for
847 Spectral Discrimination of Alteration Environments on Mars. American Mineralogist,
848 103, 11-25.

849 Yant, M., Rogers, A. D., Nekvasil, H., Zhao, Y. Y. S., & Bristow, T. (2016) Spectral
850 characterization of acid weathering products on Martian basaltic glass. Journal of
851 Geophysical Research: Planets, 121(3), 516-541.

852 Xie, H. Hicks, N. Keller, G. R. Huang, H. Kreinovich, V. (2003) An IDL/ENVI implementation
853 of the FFT-based algorithm for automatic image registration. Computers and Geoscience,
854 29, 1045 – 1055.

855

856

# Figure 1

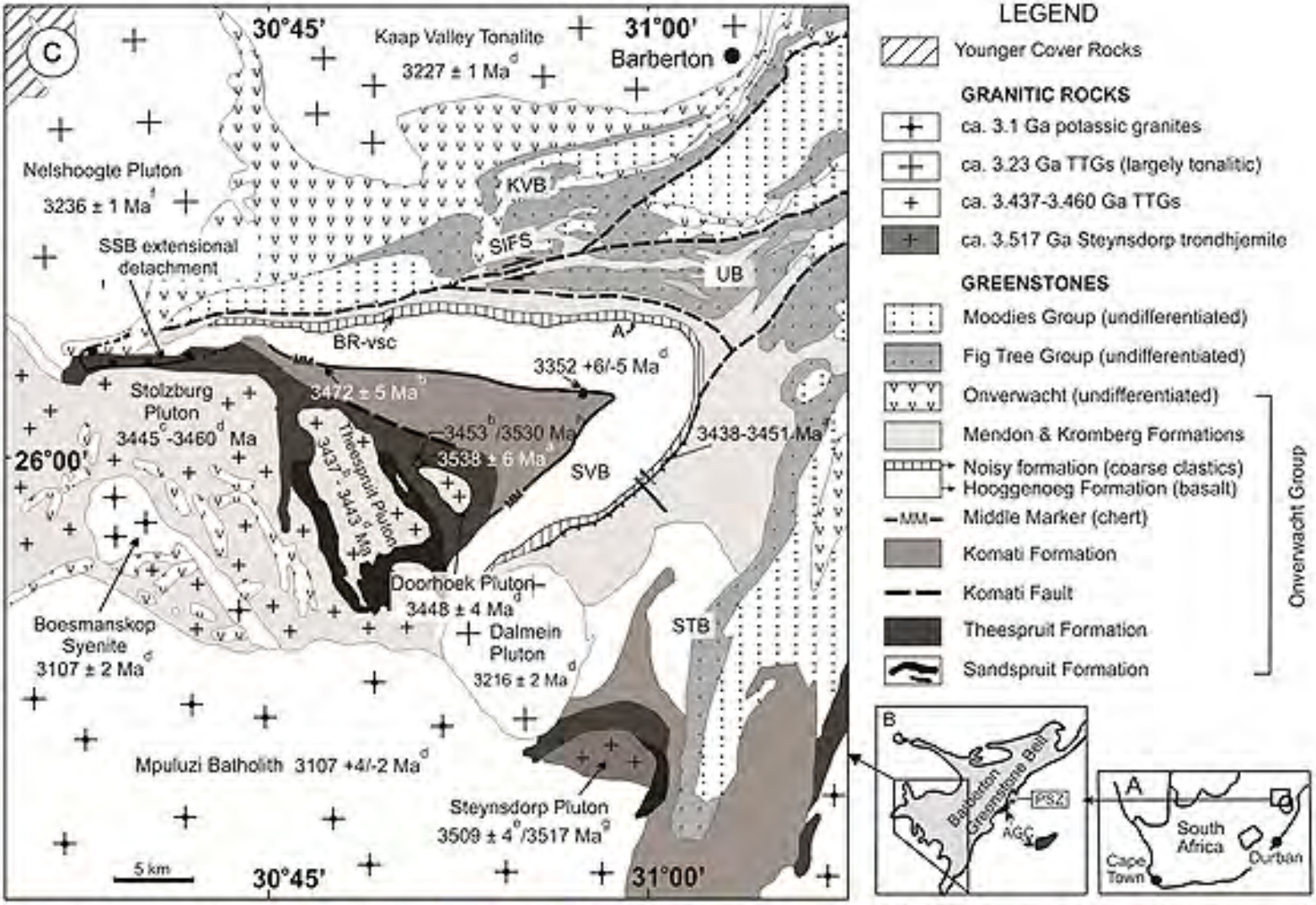
C
30°45'
31°00'
Kaap Valley Tonalite
3227 ± 1 Ma
Barberton
Nelshoogte Pluton
3236 ± 1 Ma
KVB
SSB extensional detachment
SIFS
UB
BR-vsc
A
3352 +6/-5 Ma
3472 ± 5 Ma
Stolzburg Pluton
3445 -3460 Ma
3453 /3530 Ma
3538 ± 6 Ma
3438-3451 Ma
26°00'
SVB
Theespruit Pluton
3437 - 3443 Ma
Doornhoek Pluton
3448 ± 4 Ma
Boesmanskop Syenite
3107 ± 2 Ma
Dalmein Pluton
3216 ± 2 Ma
STB
Mpuluzi Batholith 3107 +4/-2 Ma
Steynsdorp Pluton
3509 ± 4 /3517 Ma
5 km
30°45'
31°00'
LEGEND
Younger Cover Rocks
GRANITIC ROCKS
ca. 3.1 Ga potassic granites
ca. 3.23 Ga TTGs (largely tonalitic)
ca. 3.437-3.460 Ga TTGs
ca. 3.517 Ga Steynsdorp trondhjemite
GREENSTONES
Moodies Group (undifferentiated)
Fig Tree Group (undifferentiated)
Onverwacht (undifferentiated)
Mendon & Kromberg Formations
Noisy formation (coarse clastics)
Hooggenoeg Formation (basalt)
MM Middle Marker (chert)
Komati Formation
Komati Fault
Theespruit Formation
Sandspruit Formation
Onverwacht Group
B
Barberton Greenstone Belt
PSZ
AGC
A
South Africa
Cape Town
Durban


(d)


(e)


(f)


(g)

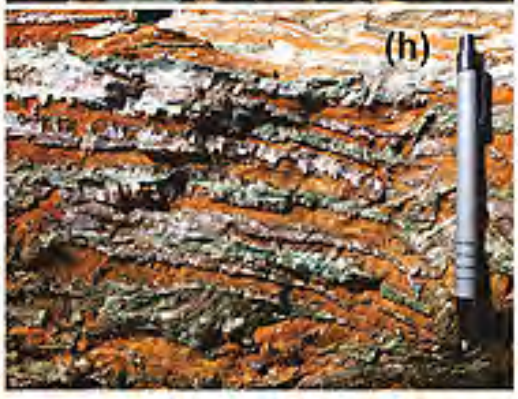
(h)

Figure 2

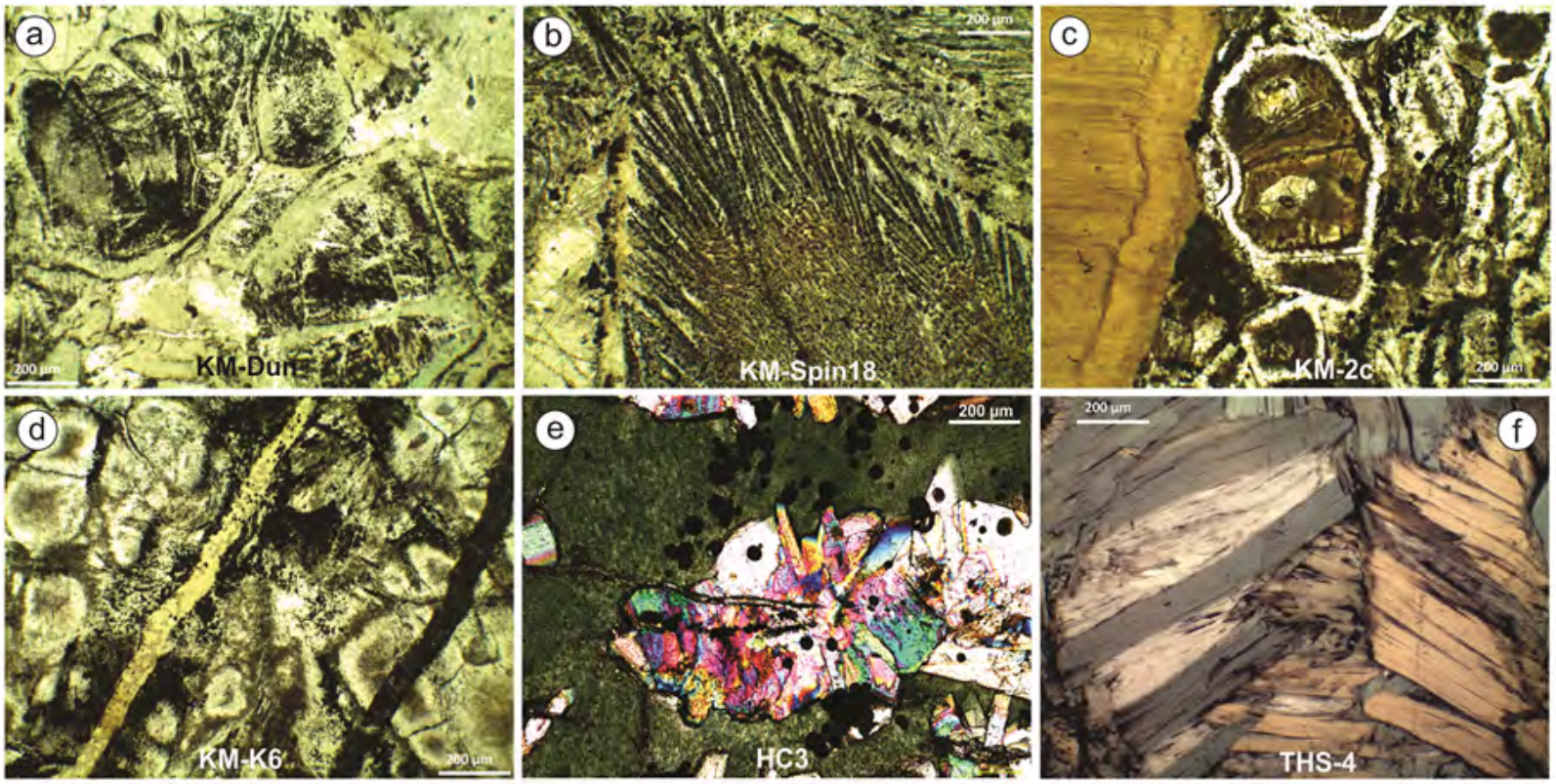
a
KM-Dun
200 µm
b
200 µm
KM-Spin18
c
KM-2c
200 µm
d
KM-K6
200 µm
e
200 µm
HC3
200 µm
f
THS-4

Figure 3

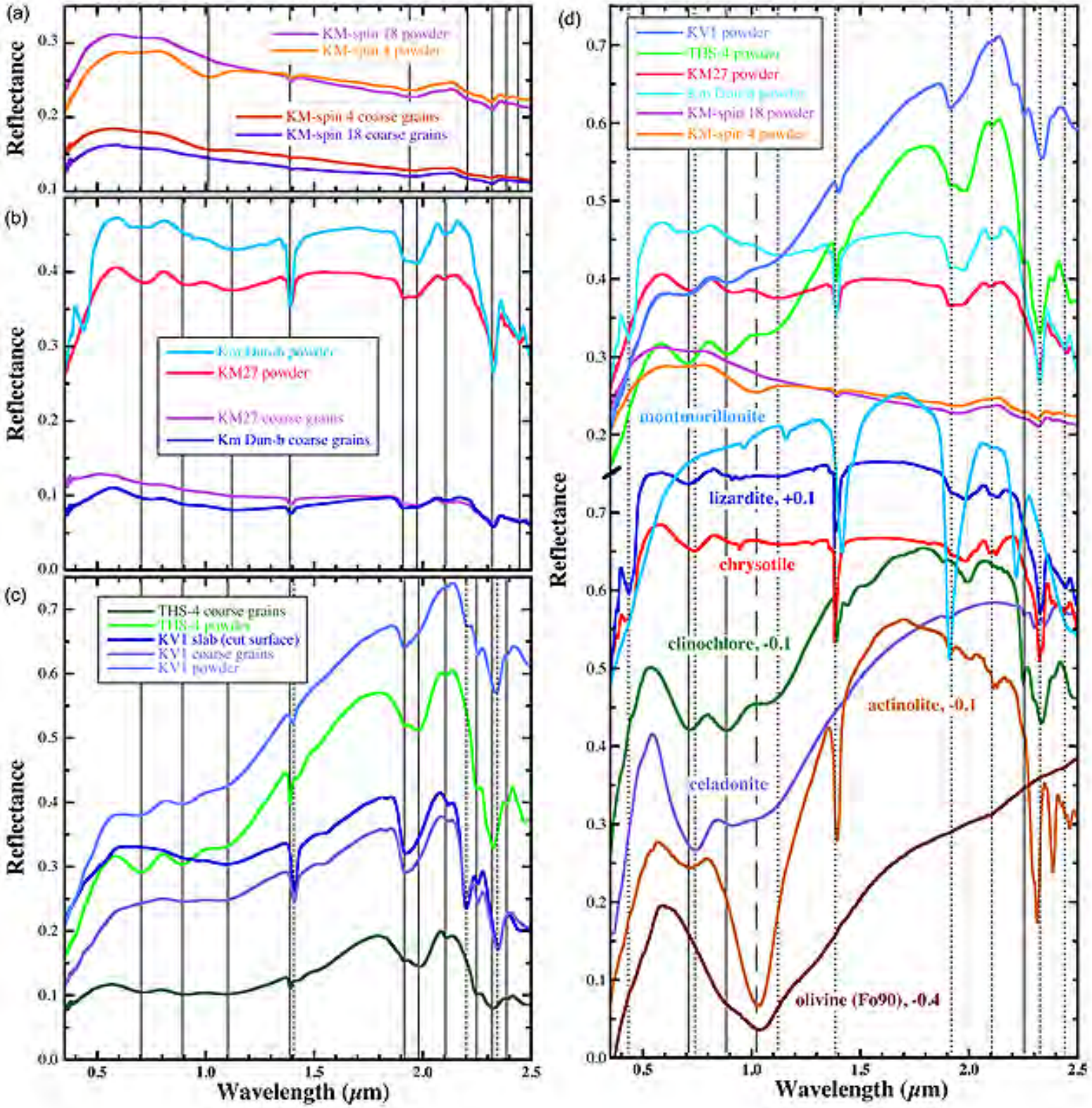
(a)
KM-spin 18 powder
KM-spin 4 powder
KM-spin 4 coarse grains
KM-spin 18 coarse grains
Reflectance
(b)
KM27 powder
KM27 coarse grains
Km Dun-b coarse grains
Reflectance
(c)
THS-4 coarse grains
KV1 slab (cut surface)
KV1 coarse grains
KV1 powder
Reflectance
Wavelength (μm)
(d)
KV1 powder
KM27 powder
KM-spin 18 powder
KM-spin 4 powder
montmorillonite
lizardite, +0.1
chrysotile
clinochlore, -0.1
actinolite, -0.1
celadonite
olivine (Fo90), -0.4
Reflectance
Wavelength (μm)

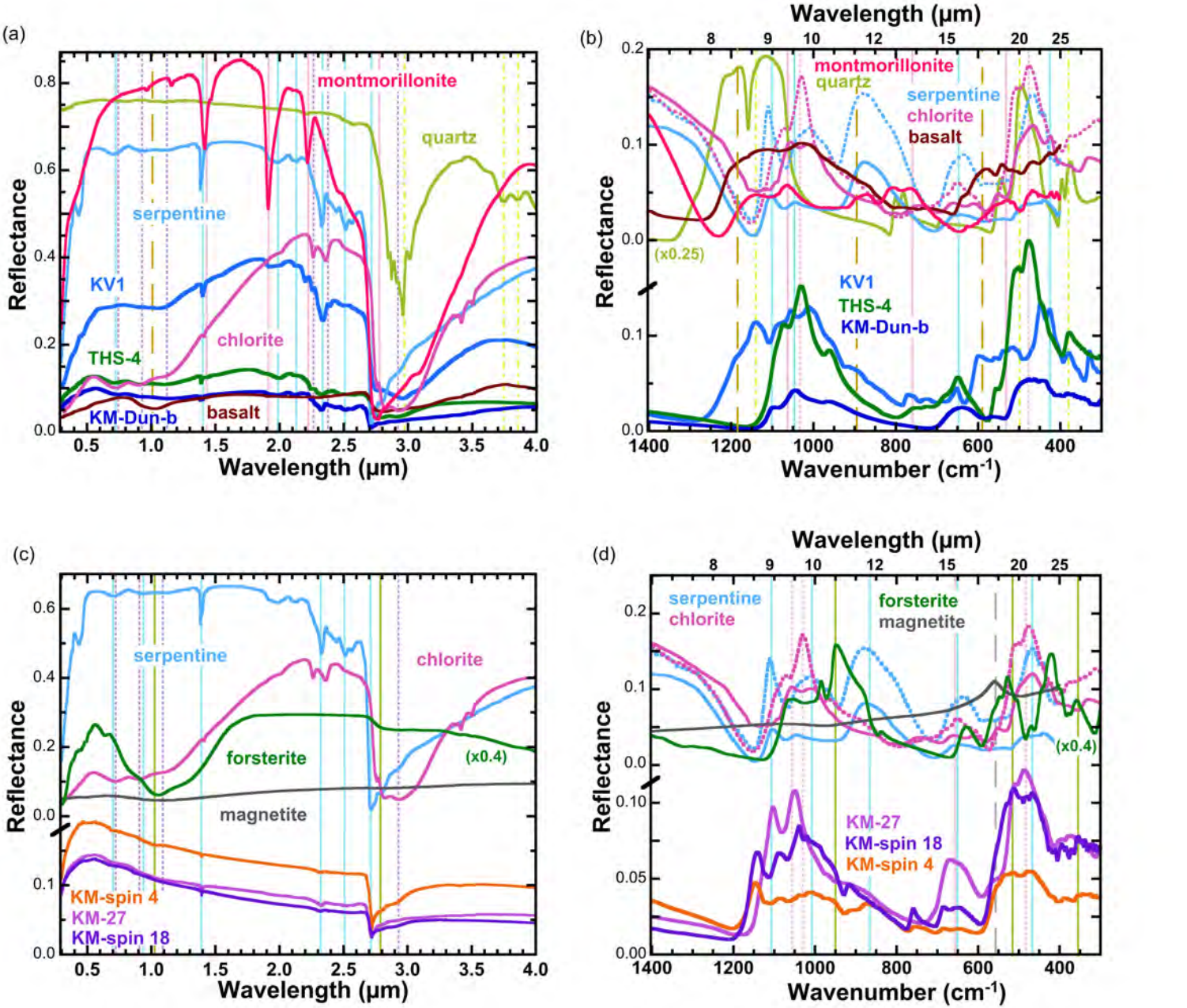
(a)
Reflectance
Wavelength (μm)
montmorillonite
quartz
serpentine
KV1
chlorite
THS-4
KM-Dun-b
basalt
(b)
Wavelength (μm)
Reflectance
Wavenumber (cm-1)
montmorillonite
quartz
serpentine
chlorite
basalt
(x0.25)
KV1
THS-4
KM-Dun-b
(c)
Reflectance
Wavelength (μm)
serpentine
chlorite
forsterite
(x0.4)
magnetite
KM-spin 4
KM-27
KM-spin 18
(d)
Wavelength (μm)
Reflectance
Wavenumber (cm-1)
serpentine
chlorite
forsterite
magnetite
(x0.4)
KM-27
KM-spin 18
KM-spin 4

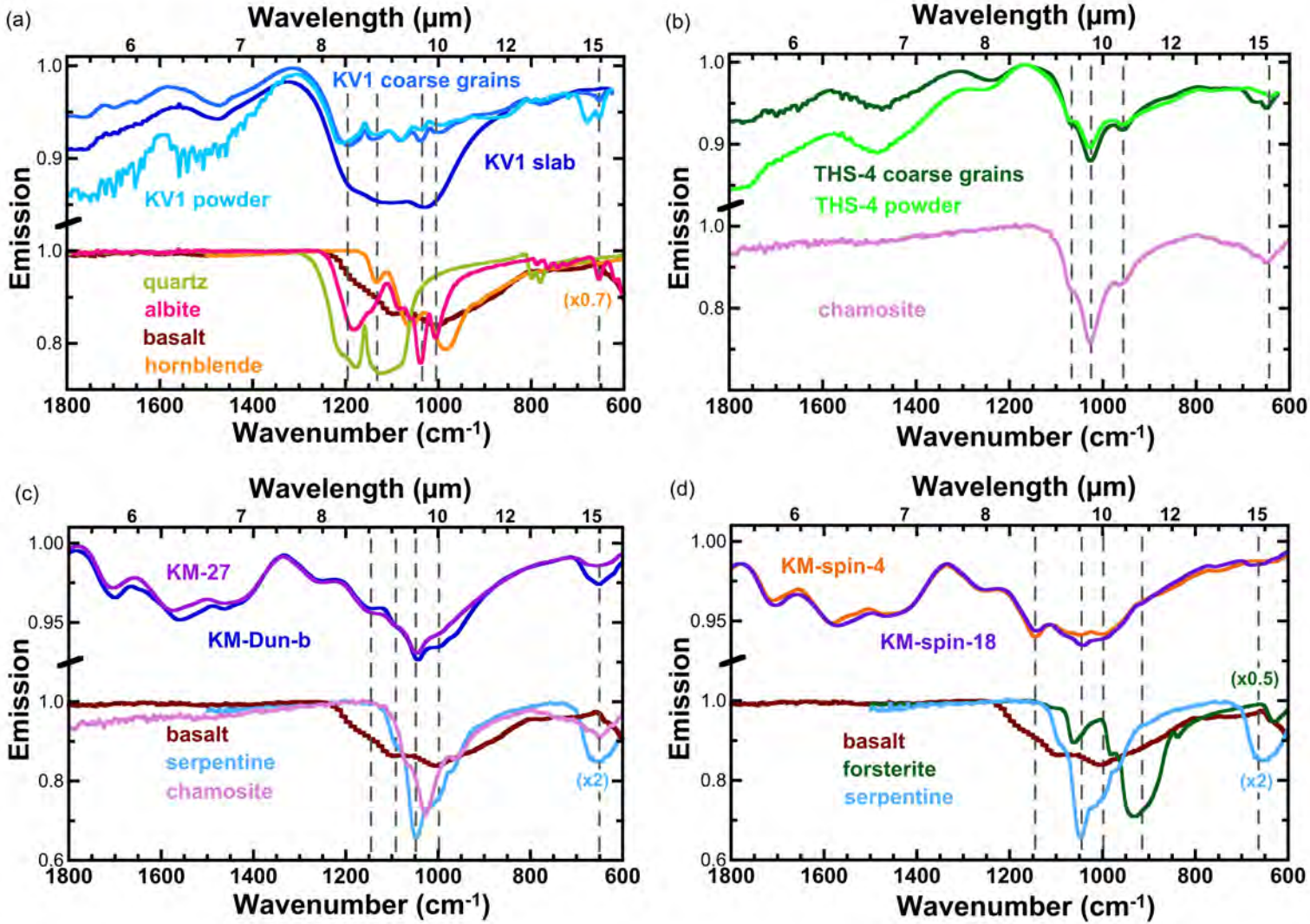
(a)
Wavelength (μm)
6
7
8
10
12
15
KV1 coarse grains
KV1 slab
KV1 powder
quartz
albite
basalt
hornblende
(x0.7)
Emission
1.0
0.9
1.0
0.8
1800
1600
1400
1200
1000
800
600
Wavenumber (cm-1)
(b)
Wavelength (μm)
THS-4 coarse grains
THS-4 powder
chamosite
(c)
Wavelength (μm)
KM-27
KM-Dun-b
basalt
serpentine
chamosite
(x2)
1.00
0.95
0.6
(d)
Wavelength (μm)
KM-spin-4
KM-spin-18
(x0.5)
basalt
forsterite
serpentine
(x2)

Figure 6

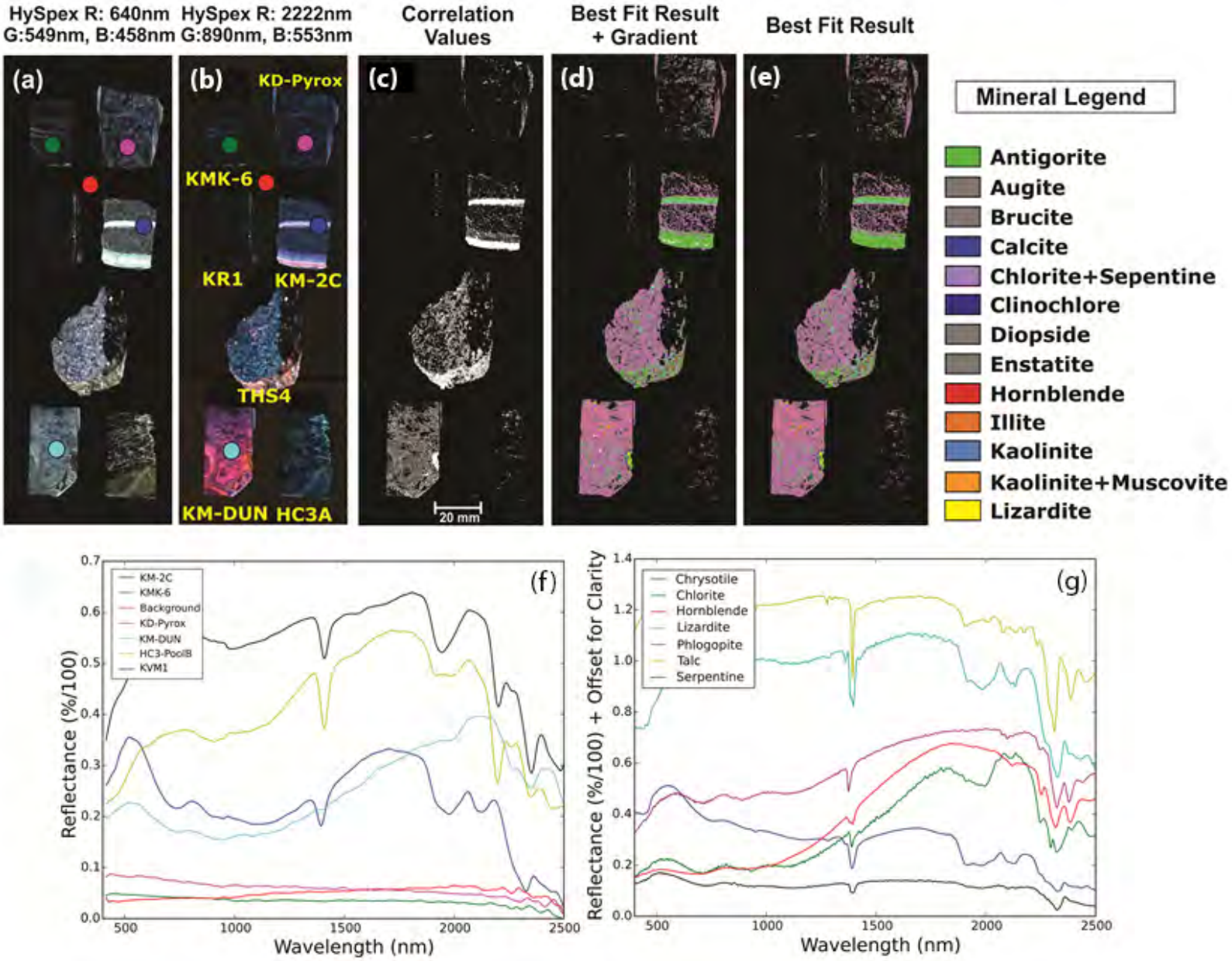
HySpex R: 640nm G:549nm, B:458nm
HySpex R: 2222nm G:890nm, B:553nm
Correlation Values
Best Fit Result + Gradient
Best Fit Result
(a)
(b)
KD-Pyrox
KMK-6
KR1
KM-2C
THS4
KM-DUN
HC3A
(c)
20 mm
(d)
(e)
Mineral Legend
Antigorite
Augite
Brucite
Calcite
Chlorite+Sepentine
Clinochlore
Diopside
Enstatite
Hornblende
Illite
Kaolinite
Kaolinite+Muscovite
Lizardite
(f)
KM-2C
KMK-6
Background
KD-Pyrox
KM-DUN
HC3-PoolB
KVM1
Reflectance (%/100)
Wavelength (nm)
(g)
Chrysotile
Chlorite
Hornblende
Lizardite
Phlogopite
Talc
Serpentine
Reflectance (%/100) + Offset for Clarity
Wavelength (nm)

Figure 7

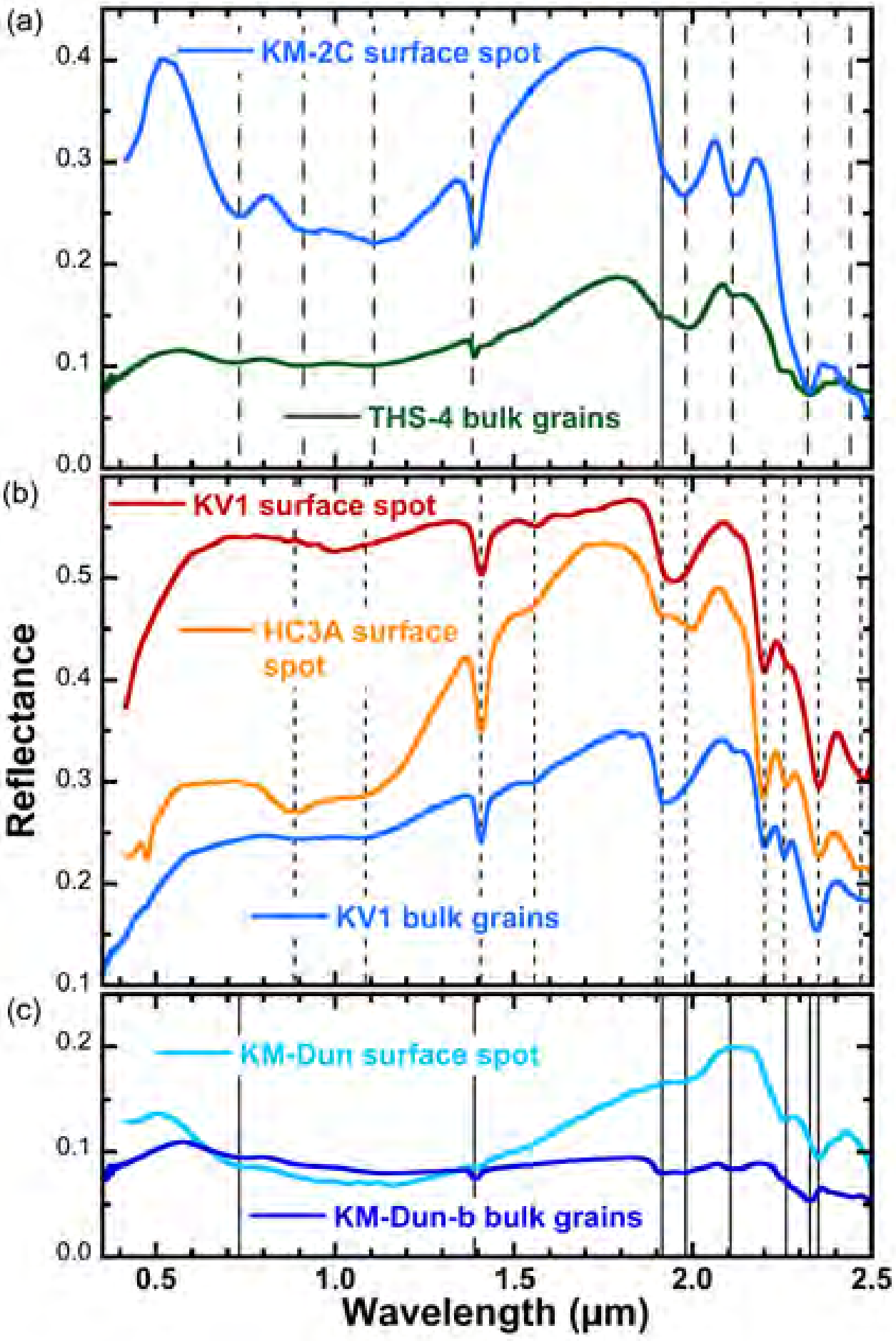
(a)
KM-2C surface spot
THS-4 bulk grains
(b)
KV1 surface spot
HC3A surface spot
KV1 bulk grains
Reflectance
(c)
KM-Dun surface spot
KM-Dun-b bulk grains
Wavelength (μm)

**Table 1.** Whole rock compositions of metabasalts

| | **Barberton** BG-196 metabasalt (this study) | [(a)] **Mars** Chesterlake metabasalt | [(a)] **Mars** Deadwood metabasalt |
|---|---|---|---|
| $SiO_2$ | 45.23 | 45.5 | 44 |
| $TiO_2$ | 1.04 | 1.09 | 0.98 |
| $Al_2O_3$ | 12.18 | 8.8 | 8.3 |
| FeOt | 20.01 | 20.10 | 19.4 |
| MnO | 0.31 | 0.48 | 0.22 |
| MgO | 9.96 | 8.8 | 5.7 |
| CaO | 8.1 | 6.8 | 6.7 |
| $Na_2O$ | 0.68 | 2.7 | 2.2 |
| $K_20$ | 0.81 | 0.41 | 0.62 |
| $P_2O_5$ | 0.06 | 1 | 0.78 |
| L.O.I | 2.2 | na | na |
| SUM | 100.58 | na | na |

[(a)] *rock compositional data from Squyres et al., 2012*

**Table 2.** List of analoge samples used in the study and there l

| Acronym | Rock type/Mineralogy |
|---|---|
| THS-4 | Greenschist facies pillow metabasite |
| KR1 | Serpentinized komatiitic basalt |
| KM-2C | Serpentine veined komatiitic basalt |
| KMK-6 | Serpentinized massive komatiite |
| KM-Spin 4 | Serpentinized Olivine Spinifex Komatiite |
| KM-Spin 18 | Serpentinized Olivine Spinifex Komatiite |
| KD-Pyrox | Altered Pyroxene Komatiite |
| KM-Dun-b | Serpentinized Metadunite |
| KM-27 | Serpentinized Massive Komatiite |
| HC3A | Greenschist facies thoeliitic basalt |
| KV1 | Altered felsic tonalite |

ocation in the Barberton greenstone belt

| Formation | AGE (Ga) | S coordinates | E coordinates |
|---|---|---|---|
| Middle Theespruit Formation | 3.53 | 25º59.854' | 030º50.191' |
| Lowermost Komati Formation | 3.48 | 25º59.586 | 030º51.094' |
| Lowermost Komati Formation | 3.48 | 25º59.582' | 030º51.098' |
| Lower Komati Formation | 3.48 | 25º59.557' | 030º51.093' |
| Lower Komati Formation | 3.48 | 25º59.569' | 030º51.088' |
| Lower Komati Formation | 3.48 | 25º59.319' | 030º51.507' |
| Middle Komati Formation | 3.48 | 25º59.264' | 030º51.564' |
| Upper Komati Formation | 3.48 | 25º58.912' | 030º50.677' |
| Upper Komati Formation | 3.48 | 25º58.837' | 030º52.035' |
| Lower Hooggenoeg Formation | 3.47 | 25º56.712' | 030º53.064' |
| TTG pluton | 3.23 | 25º44.398' | 030º59.902' |

Table 3. Spectral measurements of samples

| Sample ID | JB sample # | sample type | mineralogy | HySpex imagery | ASD | RELAB | Emission |
|---|---|---|---|---|---|---|---|
| KV1 | JB1570 | rock slab | plagioclase, quartz | X | X | | X |
| KV1 | JB1571 | coarse grains (~1 mm) | hornblende & | | X | X | X |
| KV1 | JB1572 | powder (~<125 µm) | chlorite | | X | | X |
| THS-4 | | rock slab | chlorite & | X | | | |
| THS-4 | JB1573 | coarse grains (~1 mm) | fuchsite mica | | X | X | X |
| THS-4 | JB1574 | powder (~<125 µm) | | | X | | X |
| KM-Dun | | rock slab | serpentine & magnetite | X | | | |
| KM-Dun-b-01 | JB1676 | coarse grains (~1 mm) | | | X | X | X |
| KM-Dun-b-01 | JB1677 | powder (~<125 µm) | | | X | | |
| KM-27 | JB1678 | coarse grains (~1 mm) | serpentine & chlorite | | X | X | X |
| KM-27 | JB1679 | powder (~<125 µm) | | | X | | |
| KM-spin-4 | JB1680 | coarse grains (~1 mm) | serpentine, magnetite | | X | X | X |
| KM-spin-4 | JB1681 | powder (~<125 µm) | olivine | | X | | |
| KM-spin-18 | JB1682 | coarse grains (~1 mm) | serpentine, magnetite | | X | X | X |
| KM-spin-18 | JB1683 | powder (~<125 µm) | olivine | | X | | |
| KMK-6 | | rock slab | serpentine, peridotite | X | | | |
| KD-pyrox | | rock slab | serpentine | X | | | |
| KR1 | | rock slab | serpentine, chlorite | X | | | |
| KM-2C | | rock slab | serpentine, | X | | | |
| HC3A | | rock slab | chlorite, epidote, quartz | X | | | |